

Portland State University

**PDXScholar**

---

Mechanical and Materials Engineering Faculty  
Publications and Presentations

Mechanical and Materials Engineering

---

10-2023

# A One-Dimensional Volcanic Plume Model for Predicting Ash Aggregation

D. W. Hoffman  
*Stanford University*

L. G. Mastin  
*United States Geological Survey, Cascades Volcano Observatory, Vancouver, WA*

Alexa R. Van Eaton  
*U.S. Geological Survey, Cascades Volcano Observatory*

Stephen Solovitz  
*Washington State University Vancouver*

Raul Bayoan Cal  
*Portland State University, rcal@pdx.edu*

*See next page for additional authors*

Follow this and additional works at: [https://pdxscholar.library.pdx.edu/mengin\\_fac](https://pdxscholar.library.pdx.edu/mengin_fac)



Part of the [Mechanical Engineering Commons](#)

**Let us know how access to this document benefits you.**

---

## Citation Details

Hoffman, D. W., Mastin, L. G., Van Eaton, A. R., Solovitz, S. A., Cal, R. B., & Eaton, J. K. (2023). A one-dimensional volcanic plume model for predicting ash aggregation. *Journal of Geophysical Research: Solid Earth*, 128, e2023JB027002. <https://doi.org/10.1029/2023JB027002>

This Article is brought to you for free and open access. It has been accepted for inclusion in Mechanical and Materials Engineering Faculty Publications and Presentations by an authorized administrator of PDXScholar. Please contact us if we can make this document more accessible: [pdxscholar@pdx.edu](mailto:pdxscholar@pdx.edu).

---

**Authors**

D. W. Hoffman, L. G. Mastin, Alexa R. Van Eaton, Stephen Solovitz, Raul Bayoan Cal, and J. K. Eaton

# JGR Solid Earth

## RESEARCH ARTICLE

10.1029/2023JB027002

### Key Points:

- A new 1D plume model predicts the evolution of ash size distribution due to aggregation
- Analysis incorporates a new sticking efficiency model based on novel turbulence tower experiments
- Application to a 2009 eruption of Redoubt Volcano displays a similar distribution peak and width to field measurements, albeit shifted larger

### Correspondence to:

S. A. Solovitz,  
stevesol@wsu.edu

### Citation:

Hoffman, D. W., Mastin, L. G., Van Eaton, A. R., Solovitz, S. A., Cal, R. B., & Eaton, J. K. (2023). A one-dimensional volcanic plume model for predicting ash aggregation. *Journal of Geophysical Research: Solid Earth*, 128, e2023JB027002. <https://doi.org/10.1029/2023JB027002>

Received 30 APR 2023

Accepted 20 JUL 2023




### Author Contributions:

**Conceptualization:** D. W. Hoffman, L. G. Mastin, A. R. Van Eaton, S. A. Solovitz, R. B. Cal, J. K. Eaton  
**Formal analysis:** D. W. Hoffman, L. G. Mastin, A. R. Van Eaton, S. A. Solovitz, R. B. Cal, J. K. Eaton  
**Funding acquisition:** S. A. Solovitz, R. B. Cal, J. K. Eaton  
**Investigation:** D. W. Hoffman  
**Methodology:** D. W. Hoffman, L. G. Mastin, A. R. Van Eaton, S. A. Solovitz, R. B. Cal, J. K. Eaton  
**Software:** D. W. Hoffman, L. G. Mastin, J. K. Eaton  
**Supervision:** S. A. Solovitz, J. K. Eaton  
**Validation:** D. W. Hoffman, J. K. Eaton

© 2023 The Authors. This article has been contributed to by U.S. Government employees and their work is in the public domain in the USA.

This is an open access article under the terms of the [Creative Commons Attribution-NonCommercial License](#), which permits use, distribution and reproduction in any medium, provided the original work is properly cited and is not used for commercial purposes.

## A One-Dimensional Volcanic Plume Model for Predicting Ash Aggregation

D. W. Hoffman<sup>1</sup>, L. G. Mastin<sup>2</sup> , A. R. Van Eaton<sup>2</sup> , S. A. Solovitz<sup>3</sup> , R. B. Cal<sup>4</sup>, and J. K. Eaton<sup>1</sup>

<sup>1</sup>Department of Mechanical Engineering, Stanford University, Stanford, CA, USA, <sup>2</sup>U. S. Geological Survey, Cascades Volcano Observatory, Vancouver, WA, USA, <sup>3</sup>School of Engineering and Computer Science, Washington State University Vancouver, Vancouver, WA, USA, <sup>4</sup>Department of Mechanical & Materials Engineering, Portland State University, Portland, OR, USA

**Abstract** During explosive volcanic eruptions, volcanic ash is ejected into the atmosphere, impacting aircraft safety and downwind communities. These volcanic clouds tend to be dominated by fine ash (<63 μm in diameter), permitting transport over hundreds to thousands of kilometers. However, field observations show that much of this fine ash aggregates into clusters or pellets with faster settling velocities than individual particles. Models of ash transport and deposition require an understanding of aggregation processes, which depend on factors like moisture content and local particle collision rates. In this study, we develop a Plume Model for Aggregate Prediction, a one-dimensional (1D) volcanic plume model that predicts the plume rise height, concentration of water phases, and size distribution of resulting ash aggregates from a set of eruption source parameters. The plume model uses a control volume approach to solve mass, momentum, and energy equations along the direction of the plume axis. The aggregation equation is solved using a fixed pivot technique and incorporates a sticking efficiency model developed from analog laboratory experiments of particle aggregation within a novel turbulence tower. When applied to the 2009 eruption of Redoubt Volcano, Alaska, the 1D model predicts that the majority of the plume is over-saturated with water, leading to a high rate of aggregation. Although the mean grain size of the computed Redoubt aggregates is larger than the measured deposits, with a peak at 1 mm rather than 500 μm, the present results provide a quantitative estimate for the magnitude of aggregation in an eruption.

**Plain Language Summary** Volcanic eruptions produce significant quantities of ash, which can be hazardous to aircraft and the environment. Although small ash particles can remain airborne for long distances, many fall out earlier by combining into larger clusters. The clustering process depends on many factors, notably the moisture and the turbulence within the plume. We develop a new predictive tool that models the clustering process in a volcanic plume, which includes improved estimates of the clustering behavior from new experiments with a laboratory-scale turbulence tower. We use this tool to study a 2009 eruption of Redoubt Volcano, which shows that ash particles rapidly cluster due to water within the plume. The model predicts larger clusters than observed in the field, but the estimates are improved from existing models that neglect this effect.

## 1. Introduction

During explosive volcanic eruptions, a mixture of fragmented magma and hot gases is expelled from the vent at high speed. Initially, the vertical jet is negatively buoyant, consisting mostly of solid particles of volcanic ash. The jet decelerates rapidly under the influence of gravity. The region of shear that marks the boundary between the jet and the surrounding air promotes turbulent mixing and entrainment of the ambient air (Sparks et al., 1997). Once a sufficient volume of air has been entrained and the ash cools, the mixture becomes less dense than the ambient air. At this point the inertial jet transitions to a buoyant plume. The plume continues to rise into the atmosphere by buoyant forces until the density of the surrounding atmosphere drops below that of the plume, causing the plume to decelerate until it cannot rise any higher. At the level of neutral buoyancy, ash may intrude laterally as an umbrella cloud and advect downwind to form a distal ash cloud.

The ability to predict whether fine ash disperses thousands of kilometers away or falls prematurely as aggregates has become increasingly important following the 2010 eruption of Eyjafjallajökull (Gudmundsson et al., 2012). Volcanoes located next to high-traffic airspace present a significant hazard, and inaccurate predictions of airborne

**Writing – original draft:** D. W. Hoffman, S. A. Solovitz, J. K. Eaton  
**Writing – review & editing:** L. G. Mastin, A. R. Van Eaton, R. B. Cal

ash transport can lead to overly conservative airspace closures. Field observations suggest that ash aggregation is strongly influenced by the amount of liquid water and ice present in the plume (Brown et al., 2012; Van Eaton et al., 2015). Although electrostatically bound aggregates also form in volcanic plumes, most are too fragile to preserve in ashfall deposits (Sorem, 1982). Wet and/or frozen aggregates, on the other hand, have been studied extensively as they often remain intact within the deposits long after the eruption. Understanding the formation of these aggregates is crucial to predicting where the ash is transported, since water-rich aggregates tend to settle much faster than their constitutive particles and can affect a large fraction of the erupted mass. For example, Van Eaton et al. (2015) estimated that at least 95% of fine ash (<250  $\mu\text{m}$  in diameter) was deposited as aggregates from the water-rich eruption of Redoubt Volcano, Alaska.

Some amount of moisture is always present in volcanic plumes and may originate from at least three sources: (a) water dissolved in the magma prior to eruption, (b) external water located near the vent (e.g., glacier or crater lake), and (c) humidity or precipitation in the ambient air entrained into the plume. Water in the initial plume near the vent is almost always in the vapor phase due to the high temperatures of the fragmenting magma. However, as the mixture rises and cools to the dew point temperature, the water condenses readily on ash particles, which serve as nucleation sites. For relatively dry eruptions, the mixture may rise to very high altitudes before becoming saturated and reaching the frost point temperature. If the atmosphere is dry and no water mixes with magma at the vent, the plume may be entirely under-saturated. However, volcanic ash is typically coated in hygroscopic salts, which promote water adsorption onto the particle surface even when the surrounding air is under-saturated (Delmelle et al., 2005).

Simplified plume models are useful tools for understanding how eruption source parameters may affect the amount of aggregates produced in the plume. While 1D plume models ignore spatial inhomogeneities in the radial and azimuthal directions, they capture important quantities relevant to aggregation, including plume height, water concentration, and ash volume fraction. Moreover, they can provide inputs to three-dimensional (3D) ash dispersion models, where the cells located above the vent contain concentration source terms in the advection-diffusion equations (Beckett et al., 2022). The precursor to many of the 1D plume models in use today is the cross-sectional average model of Woods (1988). Since its original introduction, a suite of 1D models has been developed, each incorporating different aspects of physical processes, including ambient cross-wind effects (Bursik, 2001), water phase transitions (Mastin, 2007; Woods, 1993), umbrella cloud formation (Folch et al., 2016), particle fallout (Bursik, 2001), and particle aggregation (Costa et al., 2010). Further details on available models are summarized in the inter-comparison study of Costa et al. (2016).

In more recent years, a major focus of plume modeling has been on the incorporation of aggregation physics. A complete description of the aggregation process requires the tracking of all particles as they combine to form new aggregates, each with a unique size and composition. Many of the earliest 1D plume models ignore the effects of aggregation altogether (Bursik, 2001; Mastin, 2007; Woods, 1993), while several recent studies have incorporated simplified aggregation physics (Beckett et al., 2022; de' Michieli Vitturi & Pardini, 2021; Folch et al., 2016). There are two numerical methods that are commonly employed in aggregation solvers. First, the fixed pivot technique (FPT) tracks the number densities of particles and aggregates in discrete bins, or pivots, with pre-defined properties (such as size and density). Costa et al. (2010) was the first to use FPT in a plume model by prescribing a single bin for the aggregates. This approach was later extended by Beckett et al. (2022) to include several bins at the expense of computational complexity. Second, the method of moments tracks the moments of aggregate property bins, and the aggregate number densities are reconstructed from these moments (de' Michieli Vitturi & Pardini, 2021).

Most recently, Beckett et al. (2022) integrated an FPT-based aggregation model into a 1D bent plume model, which was used to provide input conditions for the ash dispersion model used by the London Volcanic Ash Advisory Center. The analysis employed a similar aggregation model to Costa et al. (2010), although more flexibility was considered for the empirical fit parameters related to sticking efficiency. Through a sensitivity study, Beckett et al. (2022) found that the aggregation process was strongly dependent on these fit parameters, demonstrating that an accurate physical representation is important. They also applied their model to several eruptions of Eyjafjallajökull in 2010, which showed a modest impact on the aggregated distribution and resulting ash dispersion.

We have developed a new 1D numerical model called Plume Model for Aggregate Prediction (PMAP). The physics of plume rise is treated in a manner similar to Mastin (2007), predicting liquid water condensation and ice nucleation within the plume as a function of height along the plume centerline. Our aggregation framework uses FPT, but the chosen arrangement of bins provides greater fidelity compared to the previous approaches. The

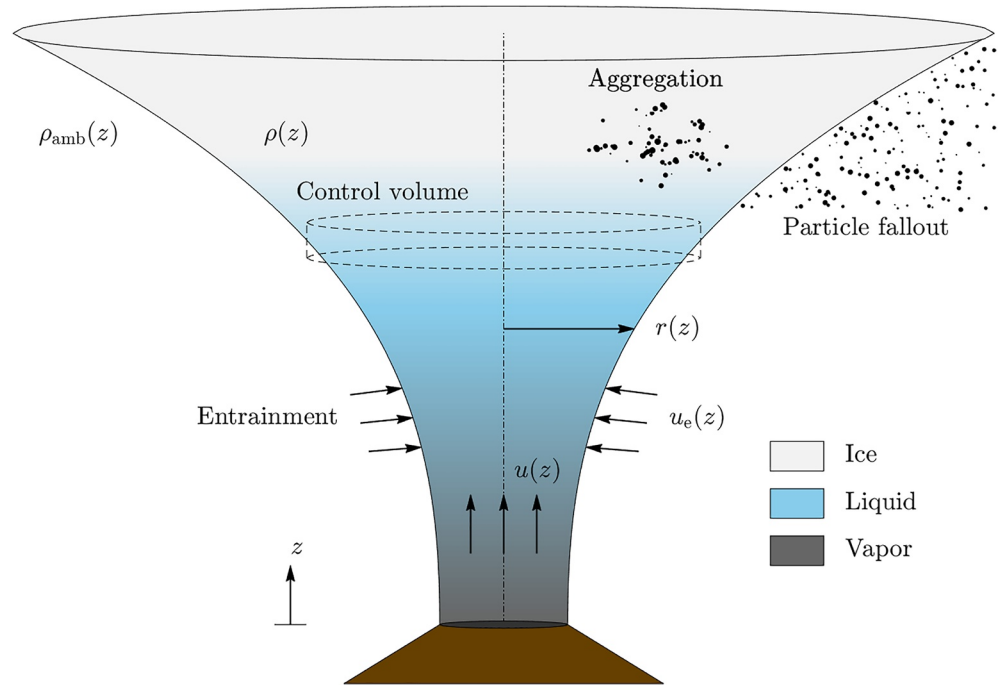


**Figure 1.** Schematic of 1D volcanic plume model and relevant processes.

aggregation solver also incorporates a new sticking efficiency model developed by Hoffman and Eaton (2023) based on turbulence tower experiments (Hoffman & Eaton, 2021). PMAP outputs the rate at which particles and aggregates are injected into the atmosphere as a function of elevation above the vent, which could serve as a useful input to more powerful 3D ash dispersion codes like Ash3D (Schwaiger et al., 2012). For the first time, we use this approach to model the aggregation that formed the deposits of a well-documented water-rich eruption. In previous aggregation studies, Veitch and Woods (2001) and Folch et al. (2010) considered deposits of the dry eruption of Mount St. Helens in 1980, while Beckett et al. (2022) examined the cloud of the dry phase of the Eyjafjallajökull eruption. Here, we examine Redoubt event 5 in 2009, and we compare the modeled aggregate grain size distribution (GSD) to the field observations of Van Eaton et al. (2015).

## 2. One-Dimensional (1D) Plume Model

PMAP analyzes the plume through control volume analysis, where conservation equations are applied to thin cylindrical regions of differential thickness. Effectively, these volumes extend upward in a vertical stack through the full plume. An example of one such control volume is depicted in Figure 1. This section discusses the set of equations governing ash particle transport and accumulation in the control volumes and the additional physical processes incorporated into the model, including ambient entrainment due to turbulence, phase transition, particle aggregation, and particle fallout. The core equations in the model are based on the 1D plume model Plumeria (Mastin, 2007), which performed effectively in the inter-comparison study by Costa et al. (2016).

### 2.1. Governing Equations

The equations that govern the plume are the result of several conservation laws applied to differential control volumes. The relevant theory was first developed under several simplifying assumptions by Morton et al. (1956). The first of these assumptions is that the flow rate of mass  $\dot{M}$ , momentum  $\dot{p}$ , energy  $\dot{E}$ , and all other relevant quantities are uniform across the plume at a given elevation  $z$ . These are regarded as “top-hat” functions, and the flow rates are defined as  $\dot{M} = \pi r^2 \rho u$ ,  $\dot{p} = \dot{M} u$ , and  $\dot{E} = \dot{M} (h + u^2/2 + gz)$ . Here,  $r$ ,  $\rho$ ,  $u$ , and  $h$  are the local plume radius, density, ascent velocity, and specific enthalpy, respectively. The second assumption is that the external cross-wind is weak, such that the plume is “un-bent” and rises vertically. Finally, we restrict our focus to plumes that are at steady state.

For numerical convenience, ash particles within the plume are sorted into  $N_b$  discrete bins, or pivots, based on two properties, particle mass  $M_{p,i}$  and particle density  $\rho_{p,i}$ . A description of how the pivots are defined and how the particles may transition between pivots during aggregation is provided in Section 3.2. For now, it is useful to define the bulk quantity  $\dot{M}_i(z)$  which represents the total mass of particles in pivot  $i$  that passes through a horizontal plane at elevation  $z$  per unit time.

For steady state conditions, mass conservation implies that the change in the total mass flow rate along the plume axis is balanced by a lateral exchange of ambient air mass through entrainment and particle mass through detrainment. In other words, ambient air along the plume margins is swept inward by turbulent vortices, increasing the total mass flow rate of the plume. On the other hand, aggregating particles can have larger settling velocities, so they may fall out of the plume and decrease the total mass flow rate. The number of particles per unit time and elevation that are detrained is denoted by  $\dot{n}'_{\text{detrain},i}(z)$  for pivot  $i$ . Assuming the air entrainment rate can be characterized by an inward radial velocity  $u_e$ , the mass conservation equation may be written as

$$\frac{d\dot{M}}{dz} = 2\pi r \rho_{\text{amb}} u_e - \sum_{i=1}^{N_b} (M_{p,i} + M_{\ell,i}^{\text{film}} + M_{\text{ice},i}^{\text{film}}) \dot{n}'_{\text{detrain},i} \quad (1)$$

where  $r$  is the top-hat radius of the plume,  $\rho_{\text{amb}}$  is the ambient air density,  $M_{\ell,i}^{\text{film}}$  is the mass of a liquid water film that coats a single particle in pivot  $i$ , and  $M_{\text{ice},i}^{\text{film}}$  is the mass of an ice film that coats a single particle in pivot  $i$ . Theory and experimental data suggest that  $u_e$  is proportional to the local ascent velocity  $u$  via an entrainment factor  $\alpha_e$  (Morton et al., 1956; Rouse et al., 1952). We adopt the entrainment model used by Woods (1993), which divides the plume into an inertial-thrust region ( $\rho > \rho_{\text{amb}}$ ) and a buoyant region ( $\rho \leq \rho_{\text{amb}}$ ):

$$u_e(z) = \begin{cases} \alpha_e u & \rho \leq \rho_{\text{amb}} \\ \alpha_e \sqrt{\frac{\rho}{\rho_{\text{amb}}}} u & \rho > \rho_{\text{amb}} \end{cases} \quad (2)$$

As in Woods (1993),  $\alpha_e$  is a constant value of 0.09.

Ernst et al. (1996) deduced from theory that the particle detrainment rate is proportional to the particle settling velocity  $u_{t,i}$  and particle flow rate  $\dot{n}_i = \dot{M}_i/M_{p,i}$  and inversely proportional to the plume radius and ascent velocity.

$$\dot{n}'_{\text{detrain},i} = \frac{\chi u_{t,i}}{ru} \dot{n}_i \quad (3)$$

The proportionality constant  $\chi \approx 0.23$  is used based on the analysis of Bursik et al. (1992). The particle settling velocity is  $u_{t,i} = \tau_{p,i} g$ , where  $\tau_{p,i}$  is the particle aerodynamic time constant. Given the wide range of Reynolds numbers experienced by the particles, Stokes' law can result in an overprediction for  $\tau_{p,i}$ . Instead we use the Schiller-Naumann correlation to correct for high Reynolds number effects (Schiller & Naumann, 1933).

$$\tau_{p,i} = \begin{cases} \frac{\rho_{p,i} d_{p,i}^2}{18\mu} \frac{1}{1 + 0.15 Re_{p,i}^{0.687}} & Re_{p,i} \leq 1000 \\ \left( 3.03 d_{p,i} \frac{\rho_{p,i}}{\rho_f} \right)^{1/2} & Re_{p,i} > 1000 \end{cases} \quad (4)$$

The terminal velocity is used in the definition of the Reynolds number,  $Re_{p,i} = u_{t,i} d_{p,i} / \nu$ , so the expression for  $u_{t,i}$  is implicit and solved by iteration at each control volume in the plume. Particle shape can also influence its terminal velocity, so we use a fractal aggregate model, as described in detail in Section 3.1. After particles fall out, re-entrainment into lower control volumes is ignored.

Equation 5 represents the change in the plume's momentum in the  $z$ -direction, which is balanced by the buoyancy force,

$$\frac{d\dot{p}}{dz} = -\pi r^2 (\rho - \rho_{\text{amb}}) g \quad (5)$$

where  $g = 9.81 \text{ m/s}^2$  is the acceleration due to Earth's gravity. The gravitational acceleration varies by less than 1% up to elevations of 30 km above sea level. Since this is within the range of heights reached by most Plinian eruption columns, using a constant value for  $g$  is sufficient. In addition, there is no vertical momentum term in this equation from the detrained mass, as this material has negligible velocity as it falls out of the plume.

The change in the plume's energy is balanced by the energy gained through entrainment, the energy lost by particle detrainment, and the energy loss due to radiation.

$$\frac{d\dot{E}}{dz} = 2\pi r \rho_{\text{amb}} u_e \left( h_{\text{amb}} + \frac{1}{2} u_e^2 + gz \right) - (h_{\text{m}}(T) + gz) \sum_{i=1}^{N_b} M_{p,i} \dot{n}'_{\text{detrain},i} - (h_{\ell}(T) + gz) \sum_{i=1}^{N_b} M_{\ell,i}^{\text{film}} \dot{n}'_{\text{detrain},i} - (h_{\text{ice}}(T) + gz) \sum_{i=1}^{N_b} M_{\text{ice},i}^{\text{film}} \dot{n}'_{\text{detrain},i} - 2\pi r \epsilon_{\text{rad}} \sigma (T^4 - T_{\text{amb}}^4) \quad (6)$$

The specific enthalpy of ambient air, tephra, liquid water, and ice are denoted by  $h_{\text{amb}}$ ,  $h_{\text{m}}$ ,  $h_{\ell}$ , and  $h_{\text{ice}}$ , respectively. All phases within each control volume are assumed to be at an equilibrium temperature  $T$ . There is no kinetic energy term from detrainment due to its negligible fallout velocity, but we do include the kinetic energy of the entrained mass for completeness. As noted by Woods (1988), this term is very small. In the radiation term,  $\epsilon_{\text{rad}}$  is the emissivity of the plume ( $\approx 0.9$ ) and  $\sigma = 5.67 \times 10^{-8} \text{ W/m}^2\text{K}^4$  is the Stefan-Boltzmann constant. The radiation term is almost always small compared to the entrainment energy term, but it may be significant near the vent, especially when the magma is at a very high temperature. To show this, the ratio of entrainment energy to radiation loss is computed using an ascent velocity of 100 m/s, ambient temperature of  $0^\circ\text{C}$ , and a magma temperature of  $900^\circ\text{C}$ . These values result in  $u_e = 9 \text{ m/s}$ ,  $\rho_{\text{amb}} = 1.29 \text{ kg/m}^3$ , and  $h_{\text{amb}} = -2.53 \times 10^4 \text{ J/kg}$ , which yields the ratio  $\rho_{\text{amb}} u_e h_{\text{amb}} / \epsilon \sigma (T^4 - T_{\text{amb}}^4) \approx 3$ . Technically, the 1D plume model neglects temperature variation across the plume cross section, so it may overestimate the temperature at the edges. This is relevant only very near the exit, so the influence is relatively small.

The thermodynamic properties are dependent on ambient conditions. When meteorological data are unavailable, PMAP solves for the pressure profile by integrating the equation for ambient hydrostatic pressure.

$$\frac{dP}{dz} = -\rho_{\text{amb}} g \quad (7)$$

In this analysis, the ambient density is calculated using an assumed temperature, which is usually extrapolated by integration from lapse rates at lower elevation. This temperature may also be determined using data for the Standard Atmosphere. If meteorological data are available, the measured pressure, ambient temperature, and relative humidity profiles are used. The ambient pressure and the pressure inside the plume are taken to be equal at any given elevation.

The mass fractions of air, water, and tephra inside the plume are tracked by integration of Equations 8–10:

$$\frac{dm_a}{dz} = \frac{1}{\dot{M}} (2\pi r \rho_{\text{amb}} u_e) m_a^{\text{amb}} - \frac{m_a}{\dot{M}} \frac{d\dot{M}}{dz} \quad (8)$$

$$\frac{dm_w}{dz} = \frac{1}{\dot{M}} \left[ (2\pi r \rho_{\text{amb}} u_e) m_w^{\text{amb}} - \sum_{i=1}^{N_b} M_{\ell,i}^{\text{film}} \dot{n}'_{\text{detrain},i} - \sum_{i=1}^{N_b} M_{\text{ice},i}^{\text{film}} \dot{n}'_{\text{detrain},i} \right] - \frac{m_w}{\dot{M}} \frac{d\dot{M}}{dz} \quad (9)$$

$$\frac{dm_m}{dz} = -\frac{1}{\dot{M}} \sum_{i=1}^{N_b} M_{p,i} \dot{n}'_{\text{detrain},i} - \frac{m_m}{\dot{M}} \frac{d\dot{M}}{dz} \quad (10)$$

It can be shown that the sum of Equations 8–10 is zero, which reflects the constraint  $m_a + m_w + m_m = 1$ .

Finally, we introduce a set of equations for  $\dot{n}_i(z)$ , the number of particles in pivot  $i$  that pass through a horizontal plane at elevation  $z$  per unit time.

$$\frac{d\dot{n}_i}{dz} = \frac{1}{u} \left( \frac{1}{2} \sum_{j=1}^{N_b} \sum_{k=1}^{N_b} f_{i,j,k} A_{j,k} \dot{n}_j n_k'' - \dot{n}_i \sum_{j=1}^{N_b} A_{i,j} n_j'' \right) - \dot{n}'_{\text{detrain},i} \quad (11)$$



Equation 11 involves an aggregation term and a particle detrainment term. The aggregation term is derived from the Smoluchowski equation that tracks the number of particles having a specific mass (Smoluchowski, 1918). This equation requires an aggregation kernel, which is based on the rate of collision and sticking between various particles. Here, the equation is rewritten using a discrete form rather than a continuously variable mass, sorting particle masses into a series of allowed bins (Jacobson et al., 1994). This discrete form requires knowledge of the kernel  $A_{i,j}$  to capture the relevant aggregation mechanisms. In addition, the number densities  $n_i''' = \dot{n}_i / (\pi r^2 u)$  must be computed beforehand, along with the weighting matrix  $f_{i,j,k}$  used to enforce mass conservation. More details concerning  $f_{i,j,k}$  and  $A_{i,j}$  are provided in Section 3.

## 2.2. Input Properties

The eruption source parameters provide the boundary conditions to Equations 1–11. These include vent elevation  $z_{\text{vent}}$ , eruption velocity  $u(z_{\text{vent}})$ , vent radius  $r(z_{\text{vent}})$ , magma temperature  $T_m$ , magma water content (by mass)  $m_{w,m}$ , mass fraction of external liquid water  $m_{\ell,\text{ext}}$ , mass fraction of external ice  $m_{\text{ice,ext}}$ , and parent ash GSD. Technically, these represent conditions following decompression to atmospheric conditions at the vent exit. It is assumed that all external water sources are thoroughly mixed with the eruptive mixture and reach equilibrium before computing the mass eruption rate (MER)  $\dot{M}(z_{\text{vent}})$ , momentum flow rate  $\dot{p}(z_{\text{vent}})$ , and energy flow rate  $\dot{E}(z_{\text{vent}})$ . Though there is no standard method for prescribing the eruption source parameters for a particular eruption, there are best practices which can be used to increase the certainty of the model inputs (Aubry et al., 2021). First,  $u(z_{\text{vent}})$  and  $r(z_{\text{vent}})$  are chosen to reproduce the MER estimate. Typically, we select an ascent velocity that avoids column collapse, and we adjust the radius to achieve the MER, similar to Plumeria (Mastin, 2007). Specific values are described further in Section 4. Consideration of the magma's origin is also important, as  $T_m$  may vary based on the magma composition, with typical values between 800 and 1200°C.

To derive the specific boundary conditions for  $\dot{M}(z_{\text{vent}})$ ,  $\dot{p}(z_{\text{vent}})$ , and  $\dot{E}(z_{\text{vent}})$ , the eruption source parameters may be used to determine the eruption mixture composition and density. The mass fraction of water at the vent is just a sum of the contributions from the external water sources and the magma water.

$$m_w(z_{\text{vent}}) = m_{\text{ice,ext}} + m_{\ell,\text{ext}} + m_{w,m}(1 - m_{\text{ice,ext}} - m_{\ell,\text{ext}}) \quad (12)$$

Then, the tephra mass fraction is  $m_m(z_{\text{vent}}) = 1 - m_w(z_{\text{vent}})$ , since tephra is the only other species present in the eruption mixture.

The vent specific enthalpy may then be computed by summing up the contributions from the magma and the various water sources:

$$h(z_{\text{vent}}) = (1 - m_{\text{ice,ext}} - m_{\ell,\text{ext}})m_{w,m}h_v(T_m) + m_{\ell,\text{ext}}h_{\ell}(T_{\ell,\text{ext}}) + m_{\text{ice,ext}}h_{\text{ice}}(T_{\text{ice,ext}}) + m_m h_m(T_m) \quad (13)$$

The analysis of the various thermodynamic properties is detailed in Appendix A. The specific enthalpy uses additional eruption source parameters for the water phase temperatures, specifically the external liquid water temperature  $T_{\ell,\text{ext}} = 283.15$  K and the external ice temperature  $T_{\text{ice,ext}} = 273.15$  K. The temperatures used here represent only nominal values, and they may be altered depending on the context of the specific eruption. The model allows the magma and external water to equilibrate before solving for the initial mixture temperature  $T(z_{\text{vent}})$  and water composition  $m_v(z_{\text{vent}})$  and  $m_{\ell}(z_{\text{vent}})$  using the iterative procedure described in Section A3 in Appendix A. In most cases,  $m_{\ell}(z_{\text{vent}}) = 0$ , except for excessively low  $T_m$  and/or large amounts of external water inputs.

Once the temperature, pressure, and composition are known, the density  $\rho(z_{\text{vent}})$  may be computed, as detailed in Appendix A. Again, this analysis sets  $m_a = 0$  and  $m_{\text{ice}} = 0$  at the vent. Then the MER is computed by  $\dot{M} = \pi r^2 \rho u$ . Similarly, the momentum rate is  $\dot{p} = \dot{M}u$ , and the energy rate is  $\dot{E} = \dot{M}(h + u^2/2 + gz)$ .

One last set of boundary conditions is required for the ordinary differential equations, specifically for the particle rate(s) in Equation 11. The relevant source parameter here is the parent ash GSD. This is specified as  $f_p$ , the mass fraction of parent ash particles in pivot  $i$ . The number of particles in pivot  $i$  ejected from the vent per unit time is then:

$$\dot{n}_i(z_{\text{vent}}) = \frac{f_i m_m(z_{\text{vent}}) \dot{M}(z_{\text{vent}})}{M_{p,i}} \quad (14)$$



Equations 1–11 are solved using an explicit fifth order Runge-Kutta scheme as described by Press and Teukolsky (1992). The step size is adjusted adaptively using an embedded fourth order scheme, which allows the truncation error to be estimated. The equations are integrated until the stopping condition  $u(z) < 1$  m/s is reached. This criterion is sufficient to determine the plume behavior to good accuracy, as tighter limits result in the same plume height to within  $\pm 10$  m. Without fallout or aggregation, the PMAP solutions agree with the original Plumeria model (Mastin, 2007) used for the core equations.

### 3. Aggregation Framework

This section provides the details needed to compute the particle flow rate in Equation 11, including the weighting matrix  $f_{i,j,k}$  and the aggregation kernel  $A_{i,j}$ . The aggregation process involves independent mechanisms for collisions and for sticking. Thus, the aggregation kernel may be conveniently decomposed into separate kernels,  $A_{ij} = \alpha_{ij}\beta_{ij}\Gamma_{ij}$ , where  $\alpha_{ij}$  is the sticking efficiency,  $\beta_{ij}$  is the collision efficiency, and  $\Gamma_{ij}$  is the geometric collision kernel. Sections 3.3 and 3.4 give expressions for  $\Gamma_{ij}$  and  $\alpha_{ij}$ , respectively. The collision efficiency,  $\beta_{ij}$ , is a hydrodynamic factor (Saffman & Turner, 1956), which is often absorbed into these other kernels. However, it can influence the aggregation rate under certain conditions. This term is also described in Section 3.4. The aggregation solver is verified using a simple aggregation kernel with a known analytical solution, as shown in Appendix B.

#### 3.1. Fractal Aggregates

Some aggregates may have lower effective densities than their constituent particles due to interstitial voids that exist between the particles. The density of an aggregate is known to decrease as the aggregate size increases (Gregory, 1997). This behavior is captured well by using fractal geometry to describe the aggregates. An aggregate is said to have the fractal property if the number of particles  $N_p$  contained within a sphere of radius  $R$  centered on the aggregate exhibits the following power-law behavior,

$$N_p \propto R^{D_f} \quad (15)$$

$D_f$  is often called the “fractal dimension,” and it describes how tightly the aggregate is packed. The fractal dimension is restricted to  $1 \leq D_f < 3$  for solid aggregating particles. Physically,  $D_f = 1$  means that the particles are arranged along a perfectly straight line, and  $D_f = 3$  means that the particles are miscible and coalesce. The solid particles in the ash aggregates are immiscible, and thus the actual fractal dimension is less than 3.

Rules governing the combination of particles must be defined for both mass and density properties. For aggregating particles initially in pivots  $i$  and  $j$ , the resulting aggregate must have a mass  $M_{p,i+j}$  to conserve mass:

$$M_{p,i+j} = M_{p,i} + M_{p,j} \quad (16)$$

Using the fractal scaling from Equation 15, the resulting aggregate density  $\rho_{p,i+j}$  is computed based on the ratio of combined mass to combined volume:

$$\rho_{p,i+j} = \frac{M_{p,i} + M_{p,j}}{\left[ \left( \frac{M_{p,i}}{\rho_{p,i}} \right)^{D_f/3} + \left( \frac{M_{p,j}}{\rho_{p,j}} \right)^{D_f/3} \right]^{3/D_f}} \quad (17)$$

For volcanic plumes, the most appropriate value of  $D_f$  for aggregates is still a subject for debate. Moreover, the exact value is likely dependent on the amount of liquid water present and the polydispersity of the parent ash. Folch et al. (2010) found that model predictions using  $D_f = 2.96$ – $2.99$  resulted in ash deposits that matched well with the 1980 Mount St. Helens and 1992 Crater Peak eruptions.

#### 3.2. Fixed Pivot Technique

First introduced by Kumar and Ramkrishna (1996), FPT is a numerical method commonly used to solve the Smoluchowski equation. In volcanic plumes, an enormous amount of aggregates can be produced, with no two aggregates being exactly alike. With FPT, the challenge of representing such a vast number of aggregates is made tractable by prescribing a set of pivots in which the aggregates are forced to reside. The pivots are characterized

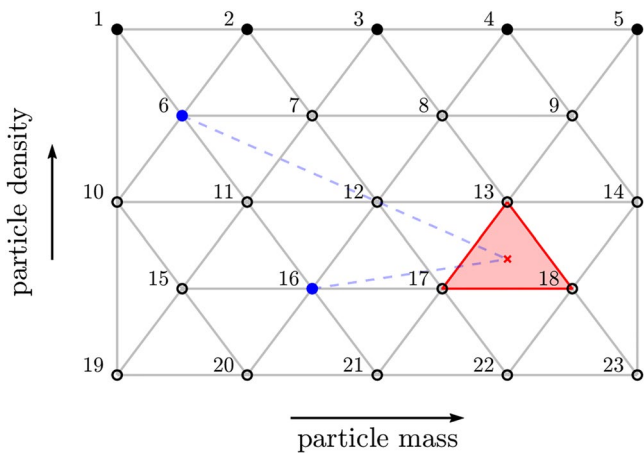


**Figure 2.** Example of numerical grid used to represent particles of varying mass and density. The row of pivots that have the highest density (filled black markers) correspond to parent particles. Two particles (or aggregates) from pivots 6 to 16 (blue markers) that combine would form a new aggregate in the highlighted cell. The mass of the new aggregate is redistributed into the adjacent pivots of that cell.

by some property, usually aggregate size or mass, and the pivot spacing may be freely altered depending on the level of accuracy desired. Rossi (2018) generalized the method to allow multiple property assignments to each pivot, and Beckett et al. (2022) used the technique in a plume model. We adopt a similar scheme, choosing mass and density as the most relevant pivot properties. In principle, other properties could be considered, such as aggregate porosity or volume.

PMAP uses a structured grid, as shown in Figure 2 for a small amount of pivots ( $N_p = 23$ ), although the method can also accommodate unstructured grids. The pivot mass increases from left to right and the pivot density increases from bottom to top. PMAP initializes particles in the top row of pivots based on the input GSD. These correspond to the highest density. As the aggregation equation is solved, the pivots with lower density and higher mass tend to become more populated as the size of aggregates increases. It is important to note that the lines connecting adjacent pivots create triangular cells, as opposed to quadrilateral cells. For two-property pivots, a triangular scheme provides the simplest map of the parameter space.

The parent GSD is a critical model input, which often comes from field measurements reported on the logarithmic Krumbein scale:

$$\phi = -\log_2\left(\frac{d_p}{1 \text{ mm}}\right) \quad (18)$$

This scaling means that a particle 1 mm in size corresponds to  $\phi = 0$ . For each unit increase or decrease in  $\phi$ , there is a respective halving or doubling of the particle size. PMAP spaces pivots in the mass direction based on this logarithmic scale. Linear spacing is used in the density direction.

As the plume develops, the particles (or aggregates) combine to form new aggregates. The resulting aggregate properties are computed from Equations 16 and 17. Unfortunately, there is an important obstacle to address, as these properties do not necessarily coincide with an existing pivot. This is illustrated in Figure 2, where the blue pivots, 6 and 16, combine to form a new aggregate of mass  $M_{p,6+16}$  and density  $\rho_{p,6+16}$ . The new aggregate, represented by the red “x” marker, falls within the shaded triangular cell, which is bounded by pivots 13, 17, and 18.

Since the numerical scheme only allows aggregates to reside in the prescribed pivots, newly formed aggregates must be redistributed into the adjacent pivots in a manner that preserves the properties of the original aggregate. This is achieved by defining a weighting matrix  $f_{i,j,k}$ , which is the fraction of aggregates that are assigned to pivot  $i$  due to a combination of particles in pivots  $j$  and  $k$ . For the example depicted in Figure 2, the three relevant weighting elements  $f_{13,6,16}$ ,  $f_{17,6,16}$ , and  $f_{18,6,16}$  are obtained by solving the following linear system:

$$\begin{pmatrix} M_{p,13} & M_{p,17} & M_{p,18} \\ \rho_{p,13} & \rho_{p,17} & \rho_{p,18} \\ 1 & 1 & 1 \end{pmatrix} \begin{pmatrix} f_{13,6,16} \\ f_{17,6,16} \\ f_{18,6,16} \end{pmatrix} = \begin{pmatrix} M_{p,6+16} \\ \rho_{p,6+16} \\ 1 \end{pmatrix}$$

These linear equations conserve the total mass, density, and aggregate fraction. Given that the number of pivots is finite, it is inevitable that some aggregates are generated that fall outside of any triangular cell. In the case that an aggregate forms outside of the right edge of the grid, the aggregate is redistributed to only the two nearest pivots. Hence, the equation preserving the mass property is dropped. Conversely, if an aggregate forms below the lowest row of pivots, the equation preserving the density property is dropped. In practice, the grid should be made large enough that only a small fraction of particles fall outside of the grid. To minimize redundant calculations, PMAP computes the entire weighting matrix once at the beginning of the analysis and stores the values in a look-up table.

### 3.3. Collision Kernel

The geometric collision kernel governs the rate at which particles in pivots  $i$  and  $j$  come into contact with one another. In this form, hydrodynamic interaction between the particles is negligible. The collision mechanisms that PMAP models include differential settling and turbulent mixing. Differential settling is a prominent mechanism in plumes where the particle suspension is highly polydisperse, given that larger particles tend to fall quickly and collide with smaller particles that are falling more slowly. Turbulent mixing can augment collisions further, especially when particle motion couples strongly with the local turbulent eddies. Other collision mechanisms could be considered, such as Brownian motion, but their impact is typically much smaller (Beckett et al., 2022; Costa et al., 2010; Textor & Ernst, 2004). PMAP assumes that the two mechanisms act independently, so their contributions to the collision kernel may be summed.

$$\Gamma_{i,j} = \pi(r_{p,i} + r_{p,j})^2 |u_{t,i} - u_{t,j}| + 2\pi(r_{p,i} + r_{p,j})^2 g_{i,j}(r_{p,i} + r_{p,j}) w_{i,j} \quad (19)$$

The first term in Equation 19 is the product of the collision cross-sectional area with the difference in settling velocities. Here,  $r_{p,i}$  and  $u_{t,i}$  are the radius and terminal velocity, respectively, of particle  $i$ . The second term accounts for turbulent mixing of inertial particles following the results of Sundaram and Collins (1997). This includes a collision enhancement factor  $g_{i,j}$  and a mean collision speed due to the turbulence  $w_{i,j}$ .

Both  $g_{i,j}$  and  $w_{i,j}$  depend on the particle aerodynamic Stokes number  $St_{\eta,i} = \tau_{p,i}/\tau_{\eta}$ . Here,  $\tau_{p,i}$  is the particle response time given by Equation 4, while  $\tau_{\eta} = \sqrt{\nu/\epsilon}$  is the Kolmogorov time scale for the smallest turbulent eddies (Kolmogorov, 1941). When  $St_{\eta,i} = 0$ , the particles track the instantaneous flow field exactly. When  $St_{\eta,i} \rightarrow \infty$ , the particles behave ballistically. In volcanic plumes, Stokes numbers can vary over a wide range, with values well below and above one in different regions. However, when  $St_{\eta,i} \approx 1$ , the particles tend to form filament-like structures at convergence zones in the turbulence, corresponding to regions of high strain. This effect is known as preferential concentration, and it can play an important role in accelerating particle aggregation (Eaton & Fessler, 1994). The collision enhancement factor,  $g_{i,j}$ , is also known as the bidisperse radial distribution function (RDF). This parameter has close ties with preferential concentration. Conceptually,  $g_{i,j}(r)$  quantifies the likelihood of finding a particle of type  $j$  at a distance  $r$  away from a particle of type  $i$ . The function is normalized using an idealized case where all particles are scattered evenly throughout space. Hence, as a particle suspension undergoes preferential concentration, the average particle will experience a local increase in surrounding particle concentration. Then,  $g_{i,j}$  will increase above one, and the collision rate will rise accordingly.

The bidisperse RDF  $g_{i,j}$  is related to monodisperse RDFs  $g_{i,i}$  and  $g_{j,j}$  via a correlation coefficient,

$$g_{i,j}(r) = 1 + \rho_{i,j}^n \sqrt{(g_{i,i} - 1)(g_{j,j} - 1)} \quad (20)$$

The coefficient  $\rho_{i,j}^n$  depends on the ratio of particle response times,  $\phi_{i,j}$ , following the fits of Zhou et al. (2001). The monodisperse RDFs are evaluated from the power-law fits of Reade and Collins (2000):

$$\rho_{i,j}^n = 2.6e^{-\phi_{i,j}} + 0.103[1 + \tanh(\phi_{i,j} - 3)] \exp[-0.0206\phi_{i,j}] \quad (21)$$

$$\phi_{i,j} = \frac{\max[\tau_{p,i}, \tau_{p,j}]}{\min[\tau_{p,i}, \tau_{p,j}]} \quad (22)$$

$$g_{i,i}(r) = \frac{7.92St_{\eta,i}^{1.80}}{0.58 + St_{\eta,i}^{3.29}} \left(\frac{r}{\eta}\right)^{\frac{-0.61St_{\eta,i}^{0.88}}{0.33 + St_{\eta,i}^{2.38}}} \exp[-0.25r/\eta] + 1 \quad (23)$$

Finally, the collision speed  $w_{i,j}$  is computed using the Saffman-Turner limit,  $w_{i,j} = (r_{p,i} + r_{p,j})\sqrt{2\epsilon/15\pi\nu}$ . This limit assumes that both  $St_{\eta,i}$  and  $St_{\eta,j}$  are zero (Saffman & Turner, 1956). The dissipation rate  $\epsilon$  inside the plume is estimated from a scaling developed for self-similar round jets (Pope, 2000),  $\epsilon = 0.017u^3/r$ . The proportionality constant comes from the experiments of Panchapakesan and Lumley (1993). It should be noted that the expression for  $w_{i,j}$  is an under-prediction in the case of finite inertia particles. Because finite inertia particles undergo preferential concentration, they tend to migrate toward convergence zones in the turbulence. Hence, they experience a somewhat higher mean collision speed than their non-preferentially concentrated counterparts. However,

there are no reliable analytical expressions for the mean collision speed of finite inertia particles to date. In summary, the final expression for the collision kernel used by PMAP is given in Equation 24,

$$\Gamma_{i,j} = \pi (r_{p,i} + r_{p,j})^2 |u_{t,i} - u_{t,j}| + \sqrt{\frac{8\pi\epsilon}{15\nu}} (r_{p,i} + r_{p,j})^3 g_{i,j} (r_{p,i} + r_{p,j}) \quad (24)$$

where  $g_{i,j}$  is computed from Equations 20–23.

### 3.4. Sticking Efficiency

The sticking efficiency  $\alpha_{i,j}$  represents the probability that particles  $i$  and  $j$  will stick and form a new aggregate if they collide. Many plume models employ the semi-empirical sticking expression developed by Costa et al. (2010),

$$\alpha_{i,j} = \frac{1}{1 + (St_{i,j}/1.3)^{0.8}} \quad (25)$$

where  $St_{i,j}$  is the collision Stokes number, which is not to be confused with the aerodynamic Stokes number discussed in Section 3.3. The collision Stokes number quantifies the importance of the particle inertia relative to the viscous force of a water film. It can be expressed in terms of the particle properties  $M_{p,i}$  and  $r_{p,i}$ , the mean collision speed  $w_{i,j}$ , and the dynamic viscosity of water  $\mu_\ell$ :

$$St_{i,j} = \frac{w_{i,j}}{6\pi\mu_\ell} \frac{M_{p,i}M_{p,j}}{M_{p,i} + M_{p,j}} \left( \frac{r_{p,i} + r_{p,j}}{r_{p,i}r_{p,j}} \right)^2 \quad (26)$$

Similar to  $\Gamma_{i,j}$  in Section 3.3, PMAP assumes that the mean collision speed  $w_{i,j}$  receives contributions from the differential settling and turbulent mixing effects:

$$w_{i,j} = |u_{t,i} - u_{t,j}| + (r_{p,i} + r_{p,j}) \sqrt{\frac{2}{15\pi} \frac{\epsilon}{\nu}} \quad (27)$$

Equation 25 is a fit to the experimental data of Gilbert and Lane (1994), which were obtained in a recirculating wind tunnel facility at elevated humidity levels. As such, the expression is appropriate when the plume conditions coincide with the conditions in the experiment. A major limitation of Equation 25 is that there is no built-in dependency on water content. Intuitively, we would expect the sticking efficiency to increase when more liquid water is available in the plume. Instead of using the Costa sticking efficiency model, PMAP uses a more general expression that accounts for changes in water content in the plume, which is based on the theory of Ennis et al. (1991).

$$\alpha_{i,j}(t_\ell; a_1, a_2) = \frac{1}{1 + [St_{i,j}/St^*(t_\ell; a_1)]^{a_2}} \quad (28)$$

$$St^*(t_\ell; a_1) = \max \left\{ 0, 2 \ln \left( \frac{t_\ell}{a_1} \right) \right\} \quad (29)$$

In Equations 28 and 29,  $t_\ell$  is the effective water film thickness coating the particles, and the parameters  $a_1$  and  $a_2$  are fits to experimental data. The dependence on water film thickness is absorbed into the critical collision Stokes number,  $St^*$ . When  $St_{i,j} = St^*$ , the sticking efficiency is 0.5; that is, the particles are just as likely to rebound as they are to form an aggregate. As more water collects on the particles,  $St^*$  increases, and particles with higher collision inertia have a greater probability of forming aggregates. When the water content becomes very large, the sticking efficiency asymptotes to one.

A new experimental apparatus has been developed by Hoffman and Eaton (2023) for the purpose of constraining the fitting parameters  $a_1$  and  $a_2$ . The remainder of this section describes the experimental methodology at a high level to provide context for the values of  $a_1$  and  $a_2$  used by PMAP. However, we refer the reader to the original paper for a more complete description.

The experimental apparatus, called the turbulence tower, is a humidified air chamber designed to emulate conditions within the buoyant region of a volcanic plume. Several renderings of the turbulence tower from different

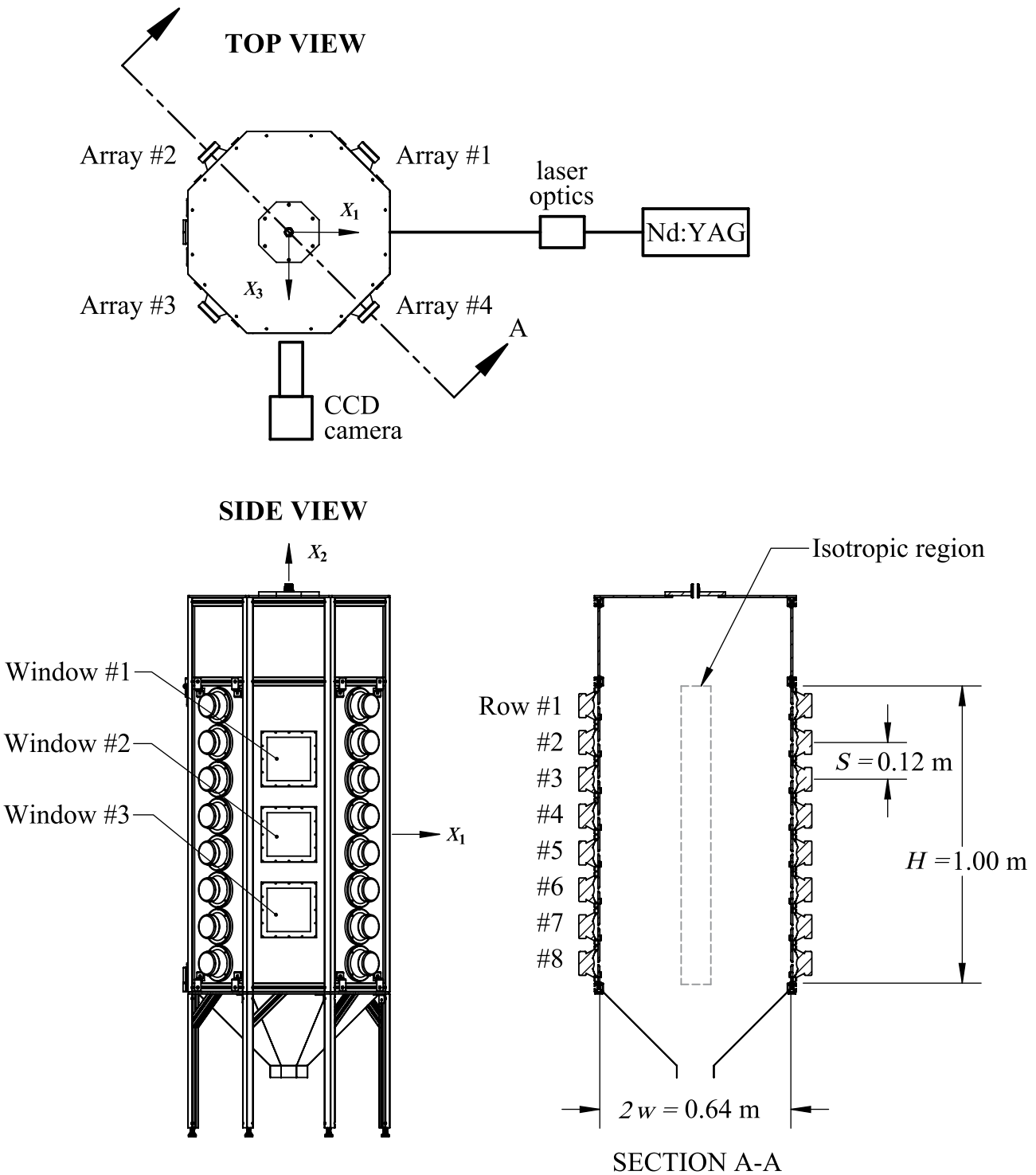


**Figure 3.** Schematic of turbulence tower as viewed from the top, side, and an oblique section that passes through the center. This figure is reproduced from Hoffman and Eaton (2021) with permission.

perspectives are shown in Figure 3. Nearly isotropic turbulence is sustained along the 1 m central axis of tower by four arrays of opposed synthetic jets. Each synthetic jet actuator is composed of a four inch woofer that drives air across a 16 mm orifice located on the wall of the tower. The turbulence injected through the jet orifice travels to the center of the tower, where it interacts with solid particles. Solid glass beads are used as a proxy for fine ash particles. The test particles have a mean diameter of 53  $\mu\text{m}$ . During each experiment, the particles drop

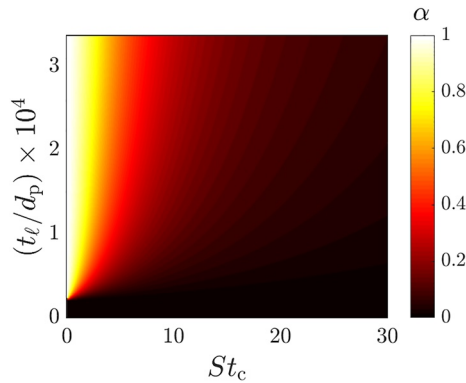


**Figure 4.** Sticking efficiency ( $\alpha$ ) map as a function of water film thickness  $t_\ell$  and collision Stokes number  $St_c$ , which was developed from the turbulence tower experiments using solid glass particles of mean diameter  $d_p = 53 \mu\text{m}$ . This figure is reproduced from Hoffman and Eaton (2023) with permission.

through the top wall of the tower due to gravity, and then they interact with the turbulence.

Particle collisions are observed individually by means of a thin laser sheet and high-speed video. A particle tracking velocimetry algorithm processes the video and predicts when a collision occurs and determines if the outcome of the collision is a rebound or an aggregation event. Once enough collisions have been observed, their corresponding collision Stokes numbers are calculated. To obtain sticking efficiency values, collisions are binned into groups according to their collision Stokes numbers, and the ratio of sticking collisions to total collisions in that bin is computed. The process is repeated for a variety of controlled relative humidities ranging from 60% to 80%. The thickness of the water film coating the particles  $t_\ell$  is inferred by comparing the wet and dry mass of physical samples that are collected as the particles and aggregates fall out of the tower. The analysis assumes a spherical shell of liquid around the particle, as typically seen in the experiments.

The data generated from the turbulence tower experiments are now in a form that enables a fit to the model given by Equations 28 and 29. The values for  $a_1$  and  $a_2$  that minimize the mean-squared-error between the model and the data are found to be 6.5 nm and 0.9, respectively. To better visualize this result, the final sticking efficiency map is plotted in Figure 4 as a function of water film thickness  $t_\ell$  and collision Stokes number  $St_{i,j}$ . These aggregation trends agree well with sampling measurements collected at the bottom of the tower. As the collision Stokes number tends to infinity,  $\alpha_{i,j}$  goes to zero, which is a feature shared by the Costa model. However, the new model exhibits an increase in sticking efficiency as the water film thickness increases. This feature presents a significant improvement over the previous model, which lacks any dependency on water content.

Volcanic plumes often rise to high elevations where the temperature is below the freezing point of water. Aggregation of ash still occurs even when ice forms on the particles and no liquid water is present (Van Eaton et al., 2015). Given the lack of experimental data related to ice aggregation, PMAP assumes a constant sticking efficiency of 0.09, similar to Costa et al. (2010). In the general case where liquid water and ice coexist, a weighted average of the two sticking efficiencies is calculated, based on the mass fraction of the phases.

In summary, the final expression for the sticking efficiency used by PMAP is given by Equations 30–33,

$$\alpha_{i,j} = \frac{m_\ell \alpha_{i,j}^\ell + m_{\text{ice}} \alpha_{i,j}^{\text{ice}}}{m_\ell + m_{\text{ice}}} \quad (30)$$

$$\alpha_{i,j}^{\text{ice}} = 0.09 \quad (31)$$

$$\alpha_{i,j}^\ell = \frac{1}{1 + [St_{i,j}/St^*(t_\ell)]^{0.9}} \quad (32)$$

$$St^*(t_\ell) = \max\left\{0, 2 \ln\left(\frac{t_\ell}{6.5}\right)\right\} \quad (33)$$

where  $t_\ell$  is in units of nm. Note that Equations 32 and 33 are exactly the same as the Costa sticking model in the case where  $t_\ell = 12.5$  nm. It is likely that this was the approximate value of the water film thickness present during the experiments of Gilbert and Lane (1994).

The collision efficiency  $\beta_{i,j}$  is the last piece of information needed to form the aggregation kernel  $A_{i,j}$ . Particles distort the flow due to their presence, which may deflect them from their original paths. This hydrodynamic interaction reduces the likelihood that particles collide. For two particles directed toward each other, the collision efficiency is the probability that they actually collide under the influence of hydrodynamic interactions (Saffman & Turner, 1956). Hoffman (2022) showed that the collision efficiency is close to 1 for ash particles greater than  $\approx 25 \mu\text{m}$  in size when settling in quiescent air (Hoffman, 2022), which encompasses a significant fraction of the mass produced in typical explosive eruptions. Therefore, PMAP ignores the effects of hydrodynamic interactions and sets  $\beta_{i,j} = 1$ .



**Table 1**  
*Eruption Source Parameters Used to Initialize Plume Model for Aggregate Prediction*

$z_{\text{vent}}$	2.2 km
$u(z_{\text{vent}})$	100 m/s
$r(z_{\text{vent}})$	110 m
$T_m$	910°C
$m_{w,m}$	0.03
$m_{e,\text{ext}}$	0
$m_{\text{ice,ext}}$	0.165
$D_f$	2.9

Electrostatic effects are not included in the sticking efficiency model. These processes depend heavily on the particle charge distribution, which is challenging to calculate. When the plume is under-saturated with water (with relative humidity below 100%), PMAP sets the sticking efficiency to zero. For this reason, PMAP should be used with caution when simulating relatively dry plumes.

#### 4. Model Performance for a Historical Eruption

The 2009 eruption of Redoubt Volcano in Alaska serves as a useful test case to evaluate the performance of PMAP for a water-rich plume. The volcanic activity of Redoubt spanned a period of 3 weeks, with 19 prominent explosive events identified by Wallace et al. (2013). The most well-documented of these events occurred on 23 March 2009 from 12:30 to 13:00 UTC and is

referred to as explosive event 5 in the eruption sequence. Ash aggregates that fell from the plume were frozen and therefore well-preserved in the deposits, allowing for measurement of both the pre-aggregation GSD and the post-aggregation GSD (Van Eaton et al., 2015).

A list of the relevant estimated eruption source parameters is provided in Table 1. The vent velocity and vent radius are primarily derived from the MER estimate. By mapping the deposits, Wallace et al. (2013) estimated the total erupted tephra mass to be  $4.4 \times 10^9$  kg. The eruption duration was  $\approx 15$  min, as inferred from the seismic records and measurements of the plume reflectivity using Doppler radar (Schneider & Hoblitt, 2013). These conditions correspond to a MER of  $4.9 \times 10^6$  kg/s. We use a vent velocity of 100 m/s, a vent radius of 110 m, and a magma mixture composed of 3% water by mass, which also produces a MER of  $4.9 \times 10^6$  kg/s. Van Eaton et al. (2015) found that aggregates from the eruption were composed of  $\sim 20\%$  water, so an additional 16.5% water (glacial ice at 0°C) is added to the initial eruption mixture. This same study also estimated a shorter eruption duration and larger MER, though this has a second-order effect on the PMAP model output, as noted later. Assuming the magmatic temperature is initially 910°C, the resulting mixture temperature is 264°C after equilibration with the ice. Ambient conditions, including pressure, temperature, and relative humidity, are obtained from a radiosonde launched from Anchorage at 12:00 UTC. This was 30 min before the start of eruptive event 5. These data are plotted in Figure 5. We use the initial GSD measured by Van Eaton et al. (2015), which has a range of  $-5 \leq \phi \leq 11$  with  $\Delta\phi = 1$ .

We used PMAP to evaluate the plume development for these source conditions. A few of the steady-state model outputs are plotted in Figure 6. These include the plume radius, ascent velocity, density, and hydrous mass fractions as a function of elevation above sea level. The model plume rises to an elevation of 16.8 km a.s.l., which is consistent with the maximum plume height of  $16 \pm 2$  km measured by radar (Mastin et al., 2013). The mixture initially decelerates due to its high density. At 500 m above the vent, the plume density falls below the ambient density, and the mixture becomes positively buoyant because of rapid entrainment. At elevations between 5 and 10 km a.s.l. the plume experiences strong vertical buoyancy-driven acceleration. The modeled plume mixture also becomes saturated with water vapor early in its ascent at a height of 5 km a.s.l. Liquid water exists in the range  $5 < z < 10$  km, liquid-ice coexists in the range  $8 < z < 10$  km, and ice is present for  $z > 10$  km. The total residence time for aggregation experienced by the ash is 4.1 min, based on the  $u(z)$  profile within the over-saturated window.

The aggregated grain size distribution (AGSD) is determined using the particles that reach the top of the plume, as well as particles detrained along the plume margins. The final aggregated size distribution is presented in Figure 7. This shows the fraction of mass contained within each of the pivots. The colored 3D surface was constructed by linear interpolation between pivots, which are also shown on the bottom surface of the figure. The modeled distribution peaks around a particle mass of 1.3 mg and a density of  $1,750 \text{ kg/m}^3$ , which corresponds to an effective diameter of 1.12 mm. The distribution peak makes a significant departure from the GSD of the parent ash, which is plotted as a gray line in Figure 7.

Next, we quantify the shift from the parent ash GSD to the final AGSD. At every pivot, the effective particle diameter is computed using the corresponding particle mass and density. Then, the mass fractions are re-assigned to  $\phi$ -bins. The resulting AGSD is plotted as a function of  $\phi$  in Figure 8. The AGSD peaks at 1.0 mm and is



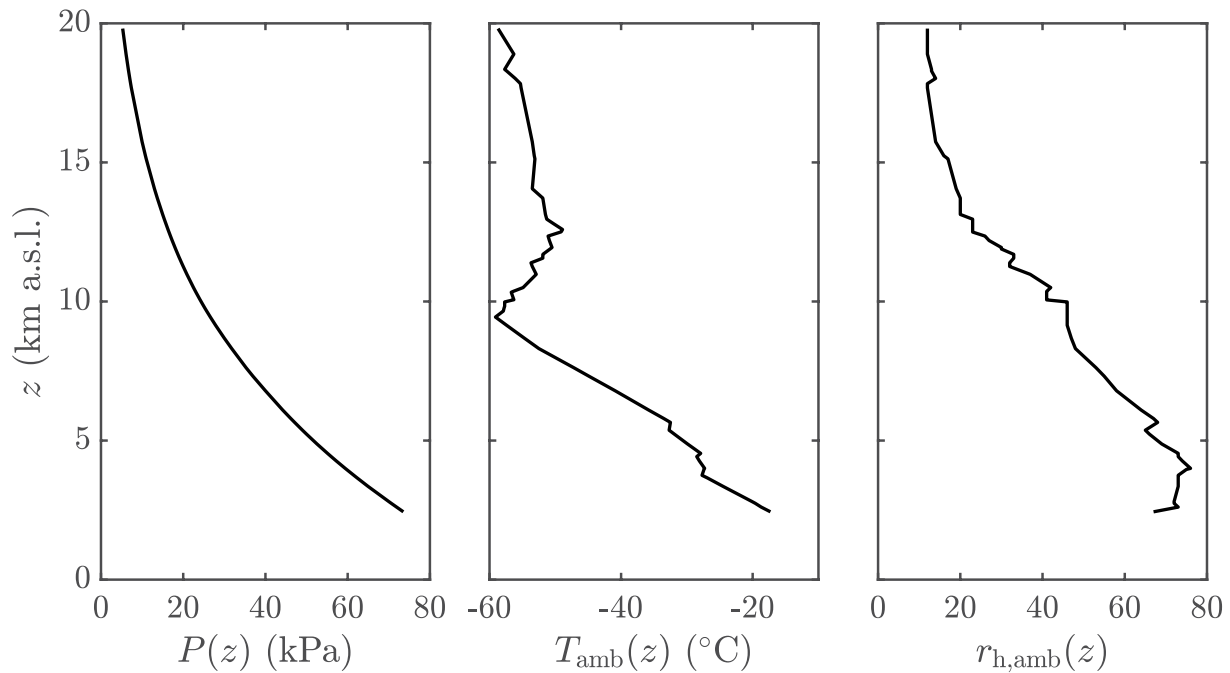


**Figure 5.** Ambient pressure, temperature, and relative humidity measured by radiosonde on 23 March 2009 at 12:00 UTC in Anchorage, Alaska, just prior to Redoubt Volcano's eruptive event 5 (source: <http://weather.uwyo.edu/upperair/sounding.html>).

noticeably narrower than the GSD. By contrast, the original GSD reaches a maximum at  $125 \mu\text{m}$ , and it is more heavily populated with fine ash. For comparison, we also generate the AGSD using the original Costa sticking model ( $St^* = 1.3$  and  $q = 0.8$ ). This produces an AGSD containing fewer large aggregates and more small aggregates relative to the baseline model. This is because the baseline sticking model predicts a higher  $St^*$  in the portion of the plume containing large amounts of liquid water, which results in sticking efficiencies closer to 1.

The distributions are also compared to the measured AGSD carried out by Van Eaton et al. (2015). The peak of the measured AGSD occurs to the left of the model predictions, indicating that the model overestimates the amount of aggregation that takes place within the plume. This same shift also occurs when using the higher MER estimated by Van Eaton et al. (2015), indicating that this is not the cause. In the model, disaggregation is ignored altogether, allowing aggregates to grow unabated.

The output AGSD is also dependent on the specific source parameters. We examine the sensitivity to two key source conditions, specifically the MER and the initial water content. All other eruption source parameters remain unchanged in these analyses. Figure 9 displays the AGSD when the MER is varied from  $4.9 \times 10^5$  to  $4.9 \times 10^7$  kg/s, extending an order of magnitude lower and higher than the original case. The effects are modest, with a gradual shift to larger aggregates at higher MER. The peak of the distribution remains at  $\phi = 0$  at lower MER, which corresponds to 1.0-mm aggregates. The shape of the distribution is nearly unchanged. Increasing the MER by an order of magnitude broadens the AGSD and shifts the peak to  $\phi = -1$ , corresponding to 2.0-mm aggregates.

The response is more sensitive to the water content. Figure 10 shows the AGSD when the initial ice mass fraction is varied from 0 to 0.20, which includes the original case at 0.165. When no water is introduced at the vent, the AGSD extends over a wide range of size classes, with mass fractions above 0.05 when  $-2 \leq \phi \leq 5$ . The peak falls within the 1-mm bin. As the water content increases, the distribution narrows, as smaller particles are aggregated to larger sizes. At an ice mass fraction of 0.15, the AGSD exceeds 0.05 only for  $-3 \leq \phi \leq 2$ . The peak remains in the same bin, though. Above the baseline case at  $m_{\text{ice,ext}} = 0.165$ , the distribution starts to shift to even larger sizes, peaking in the 2-mm bin.

This behavior suggests that the amount of water incorporated is critical to the AGSD, and it may be overestimated. Using the AGSD analyses over this range of  $m_{\text{ice,ext}}$ , the mean grain size is computed using the first moment of the

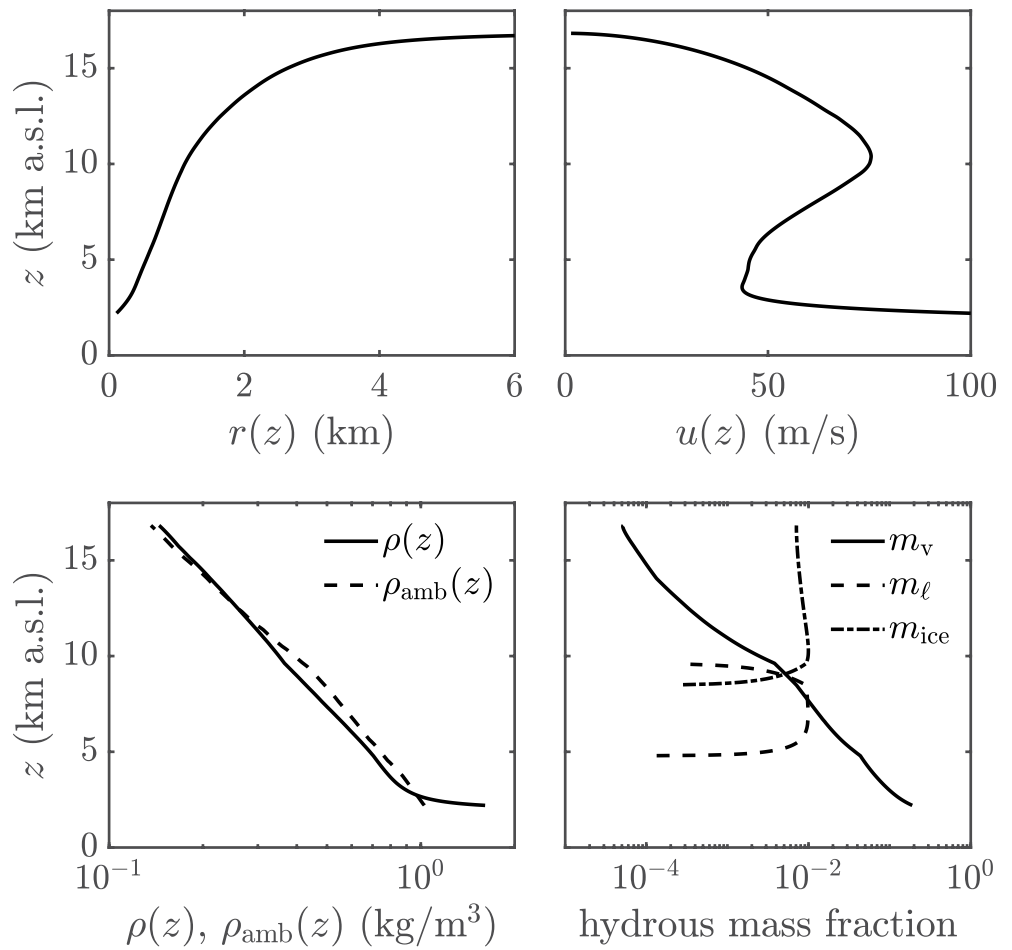


**Figure 6.** Steady state model output for plume radius, ascent velocity, density, and mass fractions of vapor, liquid water, and ice as a function of elevation above sea level for the 2009 Redoubt event 5 eruption.

mass fraction distribution. The moment is based on the linear scale, not the logarithmic Krumbein scale. Figure 11 shows the mean grain size as a function of  $m_{ice,ext}$  when both the baseline and original Costa sticking models are used.

The mean grain size from the measurement, indicated by the horizontal dashed line, is 0.97 mm. This is modestly larger than the mean grain size for the input GSD, which is 0.77 mm. Both the PMAP and Costa aggregation models consistently predict a larger mean grain size than measured. This may be due to disaggregation, as discussed later. When little or no external ice is added to the plume mixture at the vent, both aggregation models produce similar estimates. Under these conditions, the plume must cool and expand to higher elevations before reaching saturation. Hence, the window for aggregation to occur is small. For  $m_{ice,ext} > 0.04$ , the plume reaches saturation above the minimum freezing temperature, and liquid binding accelerates the growth of aggregates. Regardless of the value of  $m_{ice,ext}$ , the sticking efficiency of the baseline model generally leads to larger aggregates than the original Costa model. This is not surprising, since the original Costa model is a data fit to experiments conducted at under-saturated conditions.

It is important to note that the original Costa sticking expression produces results somewhat closer to the field observations, even if the mean grain size is still over-predicted. One possible explanation is related to the experimental data obtained by Gilbert and Lane (1994), which was used to fit the Costa

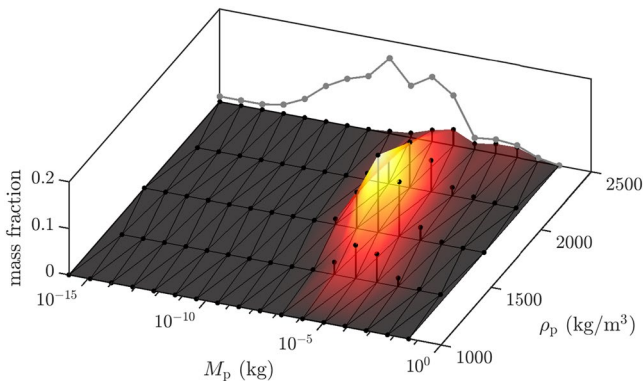


**Figure 7.** Mass fraction of ash generated by the plume contained in each pivot at the end of the analysis. Pivots vary in particle mass  $M_p$  and density  $\rho_p$ . Vertical lines denote the mass fractions in individual pivots, and color contours map the trends. The initial grain size distribution of parent ash, from Van Eaton et al. (2015), is indicated by the gray line.

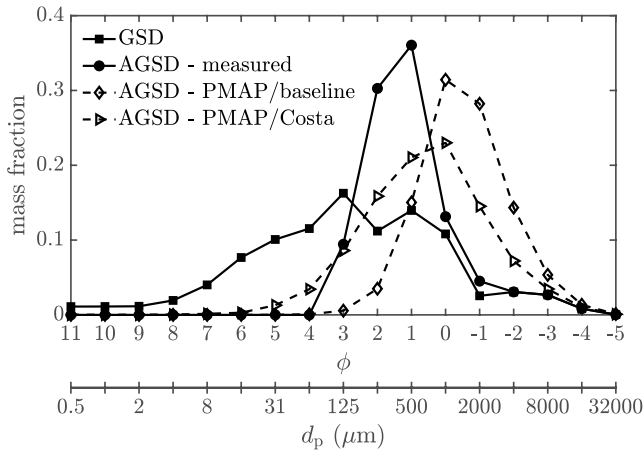


**Figure 8.** Modeled aggregated grain size distribution (AGSD) using the baseline sticking model described in Section 3.4 and the original Costa sticking model ( $St^* = 1.3$  and  $q = 0.8$ ). The measured grain size distribution and AGSD are also shown for comparison. The discrete distributions are presented using piecewise-continuous lines to help distinguish individual cases.

model. These experiments quantified the particle distributions before and after a complex process involving both aggregation and disaggregation. In other words, instead of isolating aggregation from disaggregation, the net effect of both processes was measured. We observe a similar trend with direct sampling of aggregates beneath the apparatus (Hoffman & Eaton, 2023). The bulk sticking efficiency is correspondingly lower, resulting a reduced estimate for mean grain size.

There may be potential sources of error in the measured AGSD plotted in Figure 8, which could further accentuate a discrepancy between the measurement and the model output. During sedimentation, it is possible that the ash disaggregated upon impact with the ground, which would suggest that the average grain size was larger than measured. However, there was no evidence that the largest aggregates were preferentially broken, as they were more or less intact. Also, the measurement is based on only 6 sample locations ranging from 12 to 229 km from the vent. Only one sample was collected within the aggregate isopleth that contained 83.7% of the total deposit mass (Van Eaton et al., 2015). A more diverse array of sample locations spanning the entire deposit area would greatly improve the measurement certainty. In practice, it is very difficult to get higher resolution field data before aggregates either melt out or are compromised.

It has been asserted that the collision rate in volcanic plumes is heavily dominated by the mechanism of differential settling, as opposed to turbulent mixing (Costa et al., 2010; Textor & Ernst, 2004). To evaluate this claim, the relative importance of the two collision mechanisms can be quantified by computing an aggregation rate  $\dot{M}'_{agg}$  according to Equation 34.

$$\dot{M}'_{agg} = \frac{1}{u} \sum_{i=1}^{N_b} \sum_{j=i}^{N_b} A_{i,j} \dot{n}_i n'_j (M_{p,i} + M_{p,j}) \quad (34)$$

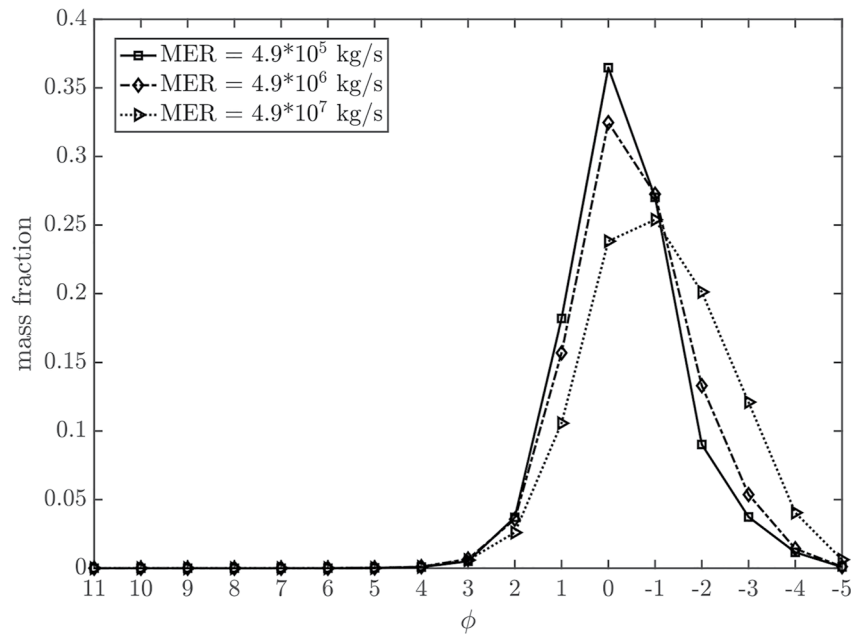


**Figure 9.** Sensitivity of modeled aggregated grain size distribution to variation in the mass eruption rate. All other parameters remain unchanged from the previous source conditions.  $\phi$  is the logarithmic Krumbein scale, where larger particles have smaller values. The discrete distributions are presented using piecewise-continuous lines to help distinguish individual cases.

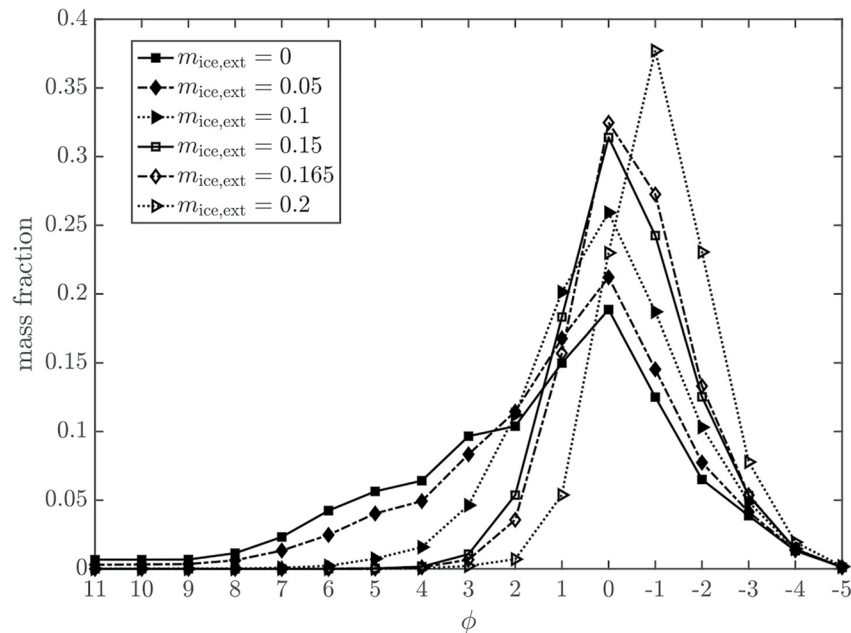


**Figure 10.** Sensitivity of modeled aggregated grain size distribution to variation in the external ice mass fraction. All other parameters remain unchanged from the previous source conditions.  $\phi$  is the logarithmic Krumbein scale, where larger particles have smaller values. The discrete distributions are presented using piecewise-continuous lines to help distinguish individual cases.

Each term in the summation represents the mass per unit time and elevation associated with the  $i$  and  $j$  particles forming new aggregates. The aggregation rate may be computed using the full aggregation kernel or a partial kernel. In the latter case, we substitute each of the two terms from Equation 19 into Equation 34 separately. The total and decomposed aggregation rates are plotted as a function of elevation in Figure 12. Since the plume is under-saturated near the vent,  $M'_{\text{agg}}$  is initially zero. At 4.5 km a.s.l., the plume first reaches the saturation point. Here, the aggregation rate is at a maximum. In fact, nearly all of the aggregation takes place within the first few hundred meters above the saturation point. This is primarily due to the high particle concentration in the lower part of the plume.

After rapid aggregation, the particle concentration is considerably lowered due to a combination of detrainment of large particles and the entrainment of ambient air. As a result, the aggregation rate remains relatively small in the middle and upper portions of the plume. The slight increase in  $M'_{\text{agg}}$  at 8 km a.s.l. coincides with the freezing point. Here, the sticking efficiency for liquid binding transitions to a constant value of 0.09. Importantly, Figure 12 supports the claim that turbulence plays a minor role in the aggregation process, at least in the 2009 Redoubt event 5 eruption. This is because the aggregation rate is nearly unchanged when the turbulent mixing term in Equation 19 is ignored.

## 5. Conclusions

A one-dimensional steady-state plume model has been developed that predicts the aggregate GSD produced in water-rich eruptions. The equation governing particle aggregation is solved using the FPT, which allows for variation in both the size and density of aggregates. The model also predicts the concentration of liquid water and ice in the over-saturated regions of the plume. This information is used to determine the type of sticking and the degree of aggregation. The sticking efficiency expression is based on a detailed suite of experiments, which use an equivalent film

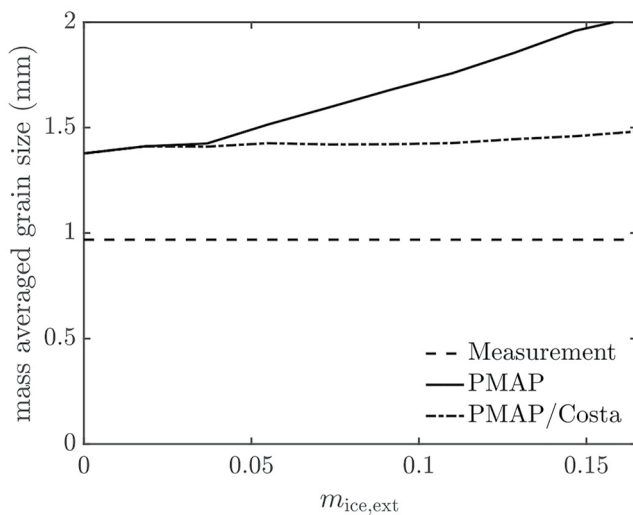


**Figure 11.** Mean grain size of aggregated ash as a function of introduced, external ice mass fraction  $m_{\text{ice,ext}}$  using the baseline and Costa sticking models for the Redoubt Volcano eruption. The mean grain size of the aggregated ash is measured to be 0.97 mm.

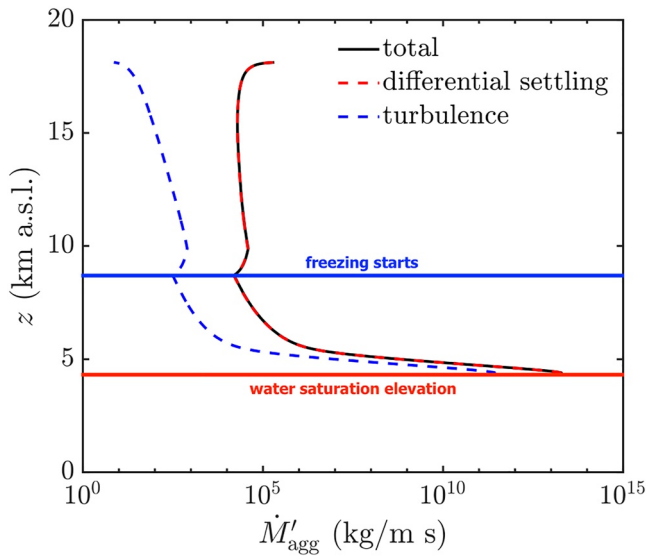


**Figure 12.** Aggregation rate as a function of elevation above sea level, computed using the full collision kernel as well as the differential settling and turbulent mixing terms. The line for differential settling overlaps with the total aggregation rate.

thickness when water exists in the liquid phase. In contrast, the original Costa sticking expression does not account for the changes in the film thickness.

The eruption of Redoubt Volcano on 23 March 2009 serves as a first test case for the model. Although the plume height is accurately predicted, the mean grain size of the aggregated ash ( $\sim 2$  mm) is over-predicted by approximately a factor of 2 compared to field observations ( $\sim 1$  mm). Almost all of the aggregation takes place within the first few hundred meters inside the saturation window. The dominant mechanism for collisions is shown to be differential settling, with the turbulent mixing mechanism contributing no more than 2% to the total aggregation rate.

Sensitivity analysis shows that the aggregated GSD is modestly dependent on MER (within the range of  $4.9 \times 10^5$  to  $4.9 \times 10^7$  kg/s), while it is strongly dependent on the water content. The mean grain size can be made to match the measured value by lowering the external ice mass fraction added at the vent. However, we used the best estimate available for the ice mass fraction. Thus, we attribute the main source of discrepancy to the fact that disaggregation is ignored. New experimental data are required to develop a disaggregation model which would limit the size of aggregates in the plume. The original Costa sticking expression remains a practical one, though it lacks the dependency on water content offered by PMAP. In fairness, both the Costa and the PMAP models are based on analog experiments of sticking efficiency. However, the Costa model uses suspended sphere data from Gilbert

and Lane (1994), which is less representative of the flow physics than the homogeneous turbulence tower of Hoffman and Eaton (2023).

Several other model limitations can affect the accuracy of the model results. Volcanic eruptions are often transient in nature, and the rise time of the plume often exceeds the eruption duration. In such cases, the steady-state model may over-estimate the degree of aggregation, as the early stages of a transient plume typically produce fewer aggregates. Spatial variations of important quantities like temperature and particle concentration in the lateral direction are also ignored in all 1D models. In reality, the outer margins of the plume become saturated before the inner core. Since the particle concentration is lowest at the margin, the top-hat representation also leads to an artificial enhancement of aggregation. Model predictions can be improved through refinement of the pivot grid, which also reduces numerical diffusion errors that over-predict large aggregates (as seen in Appendix B). An adaptive refinement technique, as described by Kumar and Ramkrishna (1996), could increase accuracy without significant computational cost in future model implementations. Finally, the contribution of electrostatics is ignored due to the lack of constraints on the particle charge distribution. Despite these current limitations, the 1D model is suitable for interfacing with existing 3D ash dispersion models. These would use local wind patterns to transform the predicted aggregate GSD into a map of regional deposits.

## Appendix A: Thermodynamic Properties

### A1. Enthalpy Functions

The specific enthalpies of dry air and the vapor, liquid, and solid phases of water are computed using the NASA polynomials given in Equation A1. The coefficients were fitted to the thermodynamic properties of each species by McBride et al. (1993), and they are listed in Table A1 for convenience:

$$\frac{h_{\text{species}}(T)}{R_{\text{species}}T} = a_1 + a_2 \frac{T}{2} + a_3 \frac{T^2}{3} + a_4 \frac{T^3}{4} + a_5 \frac{T^4}{5} + \frac{b_1}{T} \quad (\text{A1})$$

In Equation A1,  $R_{\text{species}}$  is the specific gas constant of the relevant species and  $T$  is the temperature in Kelvin. The specific enthalpy of the tephra is computed using Equation A2, assuming a constant specific heat capacity  $c_{p,m}$ :

$$h_m(T) = c_{p,m}(T - 273.15 \text{ K}) \quad (\text{A2})$$

We adopt a constant value of  $c_{p,m} = 1,100$  J/kg K used by Mastin (2007), although higher heat capacities have been measured for some magmas (Leshner & Spera, 2015).

**Table A1**  
Coefficients Defining the Specific Enthalpy for Air and Water Phases Using Equation A1, Taken From McBride et al. (1993)

		Air		Water	
		$h_a$	Vapor, $h_v$	Liquid, $h_\ell$	Ice, $h_{ice}$
$T \leq 1000$ K	$a_1$ (–)	3.5838	4.1986	$7.2558 \times 10^1$	5.2968
	$a_2$ (K <sup>-1</sup> )	$-7.2701 \times 10^{-4}$	$-2.0364 \times 10^{-3}$	$-6.6245 \times 10^{-1}$	$-6.7575 \times 10^{-2}$
	$a_3$ (K <sup>-2</sup> )	$1.6706 \times 10^{-6}$	$6.5204 \times 10^{-6}$	$2.5620 \times 10^{-3}$	$5.1694 \times 10^{-4}$
	$a_4$ (K <sup>-3</sup> )	$-1.0918 \times 10^{-10}$	$-5.4880 \times 10^{-9}$	$-4.3659 \times 10^{-6}$	$-1.4385 \times 10^{-6}$
	$a_5$ (K <sup>-4</sup> )	$-4.3178 \times 10^{-13}$	$1.7720 \times 10^{-12}$	$2.7818 \times 10^{-9}$	$1.5256 \times 10^{-9}$
	$b_1$ (K)	$-1.0505 \times 10^3$	$-3.0294 \times 10^4$	$-4.1887 \times 10^4$	$-3.6227 \times 10^4$
$T > 1000$ K	$a_1$ (–)	3.1013	2.6770	–	–
	$a_2$ (K <sup>-1</sup> )	$1.2414 \times 10^{-3}$	$2.9732 \times 10^{-3}$	–	–
	$a_3$ (K <sup>-2</sup> )	$-4.1882 \times 10^{-7}$	$-7.7377 \times 10^{-7}$	–	–
	$a_4$ (K <sup>-3</sup> )	$6.6438 \times 10^{-11}$	$9.4434 \times 10^{-11}$	–	–
	$a_5$ (K <sup>-4</sup> )	$-3.9128 \times 10^{-15}$	$-4.2690 \times 10^{-15}$	–	–
	$b_1$ (K)	$-9.8527 \times 10^2$	$-2.9886 \times 10^4$	–	–

## A2. Mixture Properties

PMAP computes the properties in each control volume assuming a homogeneous and ideal mixture. The plume density is calculated from the plume composition using Equation A3,

$$\rho = \left( \frac{(m_a R_a + m_v R_w) T}{P} + \frac{m_\ell}{\rho_\ell} + \frac{m_{ice}}{\rho_{ice}} + \frac{m_m}{\rho_m} \right)^{-1} \quad (A3)$$

where  $R_a$  and  $R_w$  are the gas constants for air and water, respectively. The component densities for liquid water, ice, and tephra are  $\rho_\ell = 1,000$ ,  $\rho_{ice} = 920$ , and  $\rho_m = 2,500$  kg/m<sup>3</sup>, respectively. The remaining parameters are the mass fractions of air  $m_a$ , water vapor  $m_v$ , liquid water  $m_\ell$ , ice  $m_{ice}$ , and magma  $m_m$ . Each of these parameters varies with elevation. The plume specific enthalpy is also calculated assuming an ideal mixture,

$$h(T) = m_a h_a(T) + m_v h_v(T) + m_\ell h_\ell(T) + m_{ice} h_{ice}(T) + m_m h_m(T) \quad (A4)$$

using the specific enthalpy of individual species provided in Equations A1 and A2 and Table A1.

## A3. Hydrous Phase Properties

PMAP predicts when the gas phase becomes saturated with water vapor, and then it computes the mass fraction of liquid water and ice species. At this condition, the phases satisfy  $m_v + m_\ell + m_{ice} = m_w$ . Liquid water is allowed to form at saturation when the mixture temperature is above  $T_{\ell,i,max} = 266.65$  K. Similarly, ice is allowed to form at saturation when the mixture temperature is below  $T_{\ell,i,min} = 258.15$  K. These two temperature criteria define the liquid-ice coexistence range, as both phases may form at temperatures  $T_{\ell,i,min} < T < T_{\ell,i,max}$ . This range is based on controlled experiments of Durant et al. (2008), who studied frozen ash samples of various compositions from multiple volcanoes.

When both ice and water are present at saturation, the partial pressure of water vapor is calculated using piecewise fits within the appropriate temperature range from Bohren and Albrecht (1998) and Haar et al. (1984):



$$P_{v,\text{sat}}(T) = \begin{cases} 611 \exp\left(22.49 - \frac{6142}{T}\right) & T \leq T_{\ell i, \text{max}} \\ 1 \times 10^5 \exp\left(6.357 - \frac{8859}{T} + \frac{607.6}{T^{0.6}}\right) & T_{\ell i, \text{max}} < T < 314 \text{ K} \\ 2.209 \times 10^7 \exp\left[\frac{T_c}{T} \sum_{i=1}^8 a_i \left(1 - \frac{T}{T_c}\right)^{\frac{i+1}{2}}\right] & T > 314 \text{ K} \end{cases} \quad (\text{A5})$$

In Equation A5,  $T_c = 647 \text{ K}$  is the critical point temperature of water, and  $a_i$  are fitting coefficients from Haar et al. (1984). These coefficients are listed in Table A2 for convenience.

The partial pressure of under-saturated water vapor is calculated using Dalton's law:

$$P_v = \frac{\frac{m_w}{M_w}}{\frac{m_a}{M_a} + \frac{m_w}{M_w}} P \quad (\text{A6})$$

where  $M_a = 28.97$  and  $M_w = 18.02 \text{ g/mol}$  are the molecular weights of dry air and water, respectively.

At saturation, the mass fraction of water vapor to dry air,  $w_{\text{sat}}$ , is calculated from the ratio of their densities through the ideal gas law:

$$w_{\text{sat}} = \frac{R_a}{R_w} \frac{P_{v,\text{sat}}}{P - P_{v,\text{sat}}} \quad (\text{A7})$$

Using Equation A7, the plume is said to be (over-)saturated when  $m_w \geq w_{\text{sat}} m_a$  and under-saturated when  $m_w < w_{\text{sat}} m_a$ .

The saturation specific enthalpy is determined by summing the enthalpy contributions at  $T_{\text{sat}}$ . Here, we assume that all of the water is in the vapor phase:

$$h_{\text{sat}} = m_a h_a(T_{\text{sat}}) + m_v h_v(T_{\text{sat}}) + m_m h_m(T_{\text{sat}}) \quad (\text{A8})$$

Due to the piecewise nature of the partial pressure expression in Equation A5, the saturation temperature  $T_{\text{sat}}$  is best solved by iteration.

At freezing temperatures, all excess water is in either liquid or ice phase. The specific enthalpies are given by Equations A9 and A10, respectively:

$$h_{\ell, \ell} = m_a h_a(T_{\ell i, \text{max}}) + m_v h_v(T_{\ell i, \text{max}}) + m_\ell h_\ell(T_{\ell i, \text{max}}) + m_m h_m(T_{\ell i, \text{max}}) \quad (\text{A9})$$

$$h_{\ell, i} = m_a h_a(T_{\ell i, \text{min}}) + m_v h_v(T_{\ell i, \text{min}}) + m_{\text{ice}} h_{\text{ice}}(T_{\ell i, \text{min}}) + m_m h_m(T_{\ell i, \text{min}}) \quad (\text{A10})$$

Liquid water and ice coexist for  $T_{\ell i, \text{min}} < T < T_{\ell i, \text{max}}$ . In this range, the relative proportion of liquid and ice is assumed to vary linearly with temperature:

$$m_\ell = (m_w - m_v) \frac{T - T_{\ell i, \text{min}}}{T_{\ell i, \text{max}} - T_{\ell i, \text{min}}} \quad (\text{A11})$$

$$m_{\text{ice}} = (m_w - m_v) \frac{T_{\ell i, \text{max}} - T}{T_{\ell i, \text{max}} - T_{\ell i, \text{min}}} \quad (\text{A12})$$

At each control volume, the integration of Equations 1–11 yields a new mixture specific enthalpy  $h$ , tephra mass fraction  $m_m$ , air mass fraction  $m_a$ , and water mass fraction  $m_w$ . The procedure for calculating the bulk mixture temperature and the hydrous phase composition within the current control volume is outlined below.

1. Guess an initial temperature  $T_g$ .
2. Calculate  $P_{v,\text{sat}}(T_g)$  from Equation A5.

**Table A2**  
Fitting Coefficients Used to Calculate Partial Pressure of Water Vapor at Saturation in Equation A5, Taken From Haar et al. (1984)

$i$	$a_i$
1	-7.8889166
2	2.5514255
3	-6.716169
4	33.239495
5	-105.38479
6	174.35319
7	-148.39348
8	48.631602



3. Use  $P_{v,\text{sat}}$  from the previous step to calculate  $w_{\text{sat}}$  using Equation A7.
4. Determine the water phase mass fractions:
  - If  $h > h_{\text{sat}}$ , the mixture is under-saturated:  $m_v = m_w$ ,  $m_\ell = 0$ , and  $m_{\text{ice}} = 0$
  - If  $h \leq h_{\text{sat}}$  and  $h \geq h_{f,\ell}$ , the mixture is saturated and all excess water is in the liquid phase:  $m_v = w_{\text{sat}}m_a$ ,  $m_\ell = m_w - m_v$ , and  $m_{\text{ice}} = 0$
  - If  $h \leq h_{\text{sat}}$  and  $h_{f,i} < h < h_{f,\ell}$ , the mixture is saturated and both ice and liquid exist:  $m_v = w_{\text{sat}}m_a$ ,  $m_\ell$  and  $m_{\text{ice}}$  from Equations A11 and A12
  - If  $h \leq h_{\text{sat}}$  and  $h \leq h_{f,i}$ , the mixture is saturated and all excess water is in the ice phase:  $m_v = w_{\text{sat}}m_a$ ,  $m_\ell = 0$ , and  $m_{\text{ice}} = m_w - m_v$
5. Use the mass fractions from the previous step and  $T_g$  to compute the resulting guess specific enthalpy  $h(T_g)$  from Equation A4.
6. Adjust  $T_g$  and repeat steps 2–5 until converged to the target specific enthalpy.

Once the hydrous mass fractions are determined, we determine the film thickness coating a single particle through conservation of mass. For both liquid water and ice films, we assume that the film thicknesses,  $t_\ell$  and  $t_{\text{ice}}$ , are the same regardless of the particle size. If a liquid water film already exists when freezing temperatures are reached, then the ice is assumed to form an outer shell around the liquid film:

$$M_{\ell,i}^{\text{film}} = \frac{4}{3}\pi \left[ (r_{p,i} + t_\ell)^3 - r_{p,i}^3 \right] \rho_\ell \quad (\text{A13})$$

$$M_{\text{ice},i}^{\text{film}} = \frac{4}{3}\pi \left[ (r_{p,i} + t_\ell + t_{\text{ice}})^3 - (r_{p,i} + t_\ell)^3 \right] \rho_{\text{ice}} \quad (\text{A14})$$

The film thicknesses  $t_\ell$  and  $t_{\text{ice}}$  depend on the hydrous mass fractions obtained in the previous step and are found by solving Equations A15 and A16 iteratively:

$$m_\ell \dot{M} = \frac{4}{3}\pi \rho_\ell \sum_{i=1}^{N_b} \dot{n}_i \left[ (r_{p,i} + t_\ell)^3 - r_{p,i}^3 \right] \quad (\text{A15})$$

$$m_{\text{ice}} \dot{M} = \frac{4}{3}\pi \rho_{\text{ice}} \sum_{i=1}^{N_b} \dot{n}_i \left[ (r_{p,i} + t_\ell + t_{\text{ice}})^3 - (r_{p,i} + t_\ell)^3 \right] \quad (\text{A16})$$

For the surrounding ambient air, the density  $\rho_{\text{amb}}$  and specific enthalpy  $h_{\text{amb}}$  are computed in a similar manner as the plume mixture:

$$\rho_{\text{amb}} = \frac{P}{(m_a^{\text{amb}} R_a + m_v^{\text{amb}} R_v) T} \quad (\text{A17})$$

$$h_{\text{amb}}(T) = m_a^{\text{amb}} h_a(T) + m_v^{\text{amb}} h_v(T) \quad (\text{A18})$$

The mass fractions of dry air and water vapor in the ambient air,  $m_a^{\text{amb}}$  and  $m_v^{\text{amb}}$  respectively, depend on the relative humidity  $r_h$ . By definition,  $r_h$  quantifies the ratio of water vapor density to dry air density relative to saturation conditions:

$$w \equiv \frac{m_v}{m_a} = r_h w_{\text{sat}} \quad (\text{A19})$$

The value of  $w_{\text{sat}}$  is calculated using Equation A7 at the ambient temperature. Then, we determine the remaining mass fractions from Equation A19 and the requirement that  $m_v^{\text{amb}} + m_a^{\text{amb}} = 1$ . These provide the details for the ambient composition.

## Appendix B: Aggregation Solver Verification

To verify the accuracy of the numerical aggregation framework, Equation 11 is solved in isolation from the other governing ordinary differential equations used in PMAP. We do not examine a specific eruption, but

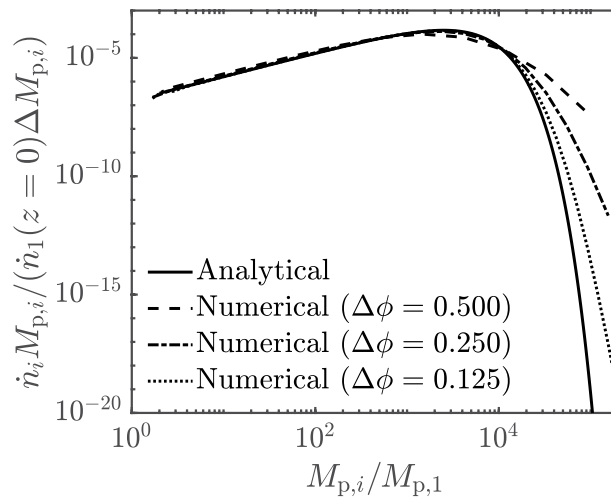


**Figure B1.** Normalized mass fraction of particles in each pivot at the end of the verification analysis compared to the true solution. This fraction is calculated by multiplying the particle rate by the particle mass and dividing by both the initial particle rate and the pivot spacing.

instead focus on a case with a known analytical solution. Rather than determining the plume ascent velocity and the plume radius from the mass, momentum, and energy equations, we set them to constant values,  $u = 50$  m/s and  $r = 50$  m. These simplifications allow for a comparison to Smoluchowski's analytical solutions (Smoluchowski, 1918) when the aggregation kernel  $A_{ij}$  is also a constant. We set this artificially to  $1 \times 10^{-9}$  m<sup>3</sup>. The erupted ash is initially monodisperse, and the particle rate of the first pivot set to  $\dot{n}_1(z = 0) = 5.0 \times 10^{-5}$  s<sup>-1</sup>. Under these conditions, the final distribution of particles leaving the plume at an elevation  $H = 10$  km is

$$\frac{\dot{n}_i(z = H)}{\dot{n}_1(z = 0)} = \frac{\left[ \frac{1}{2} \frac{H}{u} A_{i,j} n_1'''(z = 0) \right]^{i-1}}{\left[ 1 + \frac{1}{2} \frac{H}{u} A_{i,j} n_1'''(z = 0) \right]^{i+1}} \quad (\text{B1})$$

The numerical results are compared to Equation B1 in Figure B1. The quantity plotted is the normalized mass fraction. This is obtained by first multiplying the particle rate  $\dot{n}_i$  by the particle mass  $M_{p,i}$ . Then, it is normalized by the product of the initial particle rate  $\dot{n}_1(z = 0)$  and the pivot spacing  $\Delta M_{p,i}$ . Analyses are performed for several pivot spacings, specified in the legend in  $\phi$  units. For the numerical solutions, excess mass ends up in the pivots that represent larger particles, as seen in the right side of Figure B1. Similar results were obtained in the simulations of Jacobson et al. (1994), who attributed the effect to numerical diffusion. As the pivot spacing is reduced, the numerical solution converges to the analytical solution, resolving the roll-off at large aggregate sizes. Note, though, that the vertical axis in Figure B1 covers 15 orders of magnitude, so finer resolution for larger pivot indices is not necessary.

### Acronyms

AGSD	Aggregated grain size distribution
FPT	Fixed pivot technique
GSD	Grain size distribution
MER	Mass eruption rate
PMAP	Plume Model for Aggregate Prediction
RDF	Radial distribution function

### Notation

$a_1$	Film thickness fit parameter for sticking efficiency model
$a_2$	Exponent fit parameter for sticking efficiency model
$A_{i,j}$	Aggregation kernel
$c_{p,m}$	Specific heat capacity of magma

$D_f$	Fractal dimension
$d_p$	Particle diameter
$\dot{E}$	Total energy flow rate through plume, $\dot{E} = \dot{M}(h + u^2/2 + gz)$
$f_i$	Mass fraction of parent ash in bin $i$
$f_{i,j,k}$	Weighting matrix
$g$	Gravitational acceleration
$g_{i,j}$	Radial distribution function
$H$	Plume height
$h$	Bulk plume specific enthalpy
$h_a$	Specific enthalpy of dry air
$h_{amb}$	Specific enthalpy of ambient air
$h_{f,i}$	Bulk plume specific enthalpy where all excess water is ice
$h_{f,\ell}$	Bulk plume specific enthalpy where all excess water is liquid
$h_{ice}$	Specific enthalpy of ice
$h_\ell$	Specific enthalpy of liquid water
$h_m$	Specific enthalpy of tephra
$h_{sat}$	Bulk plume specific enthalpy at saturation
$h_v$	Specific enthalpy of water vapor
$\dot{M}$	Total mass flow rate through plume, $\dot{M} = \pi r^2 \rho u$
$\dot{M}'_{agg}$	Mass aggregation rate
$\dot{M}_i$	Mass flow rate of particles in bin $i$ through plume
$M_a$	Molecular weight of dry air
$M_{ice,i}^{film}$	Mass of ice coating a single particle in bin $i$
$M_{\ell,i}^{film}$	Mass of liquid water coating a single particle in bin $i$
$M_{p,i}$	Mass of a single particle in bin $i$
$M_w$	Molecular weight of water
$m_a$	Mass fraction of dry air
$m_a^{amb}$	Mass fraction of dry air in ambient atmosphere
$m_{ice}$	Mass fraction of ice
$m_{ice,ext}$	Mass fraction of external ice erupted with magma
$m_\ell$	Mass fraction of liquid water
$m_{\ell,ext}$	Mass fraction of external liquid water erupted with magma
$m_m$	Mass fraction of tephra
$m_v$	Mass fraction of water vapor
$m_v^{amb}$	Mass fraction of water vapor in ambient atmosphere
$m_w$	Mass fraction of water
$m_{w,m}$	Mass fraction of water in magma mixture
$\dot{n}'_{detrain,i}$	Detrainment rate of particles in bin $i$ per unit elevation
$\dot{n}_i$	Flow rate of particles in bin $i$ through plume
$n_i'''$	Number density of particles in bin $i$ , $n_i''' = \dot{n}_i / (\pi r^2 u)$
$N_p$	Number of pivots
$N_p$	Number of particles
$\dot{p}$	Total momentum flow rate through plume, $\dot{p} = \dot{M}u$
$P$	Jet pressure
$P_v$	Partial pressure of water vapor
$P_{v,sat}$	Partial pressure of water vapor at saturation
$q$	Collision Stokes number exponent
$R$	Sphere radius
$R_a$	Specific gas constant of dry air
$R_w$	Specific gas constant of water
$r$	Top-hat radius of plume
$r_h$	Relative humidity
$r_{p,i}$	Radius of particle $i$
$Re_{p,i}$	Reynolds number of particle in bin $i$ , $Re_{p,i} = u_{t,i} d_{p,i} / \nu$

$St_\eta$	Stokes number defined using the Kolmogorov time scale, $St_\eta = \tau_p/\tau_\eta$
$St_{i,j}$	Collision Stokes number of particles $i$ and $j$
$St^*$	Critical collision Stokes number
$T$	Temperature
$T_{amb}$	Temperature of ambient air
$T_g$	Guess temperature
$T_{ice,ext}$	Temperature of external ice added to eruption mixture
$T_{\ell,ext}$	Temperature of external liquid water added to eruption mixture
$T_{\ell_i,max}$	Maximum temperature for liquid water and ice coexistence
$T_{\ell_i,min}$	Minimum temperature for liquid water and ice coexistence
$T_m$	Magma temperature
$t_\ell$	Liquid water film thickness
$u$	Ascent velocity of plume
$u_e$	Entrainment velocity
$u_{t,i}$	Terminal velocity of particle $i$
$w$	Ratio of water vapor mass fraction to dry air mass fraction
$w_{sat}$	Ratio of water vapor mass fraction to dry air mass fraction at saturation
$w_{i,j}$	Mean collision speed of particles $i$ and $j$
$z$	Elevation above sea level
$z_{vent}$	Elevation of vent above sea level
$\alpha_e$	Entrainment factor
$\alpha_{i,j}$	Sticking efficiency
$\alpha_{i,j}^{ice}$	Sticking efficiency for ice coated particle
$\alpha_{i,j}^\ell$	Sticking efficiency for liquid coated particle
$\beta_{i,j}$	Collision efficiency
$\Gamma_{i,j}$	Geometric collision kernel for particles $i$ and $j$
$\epsilon_{rad}$	Plume emissivity
$\epsilon$	Dissipation rate of turbulence kinetic energy
$\eta$	Kolmogorov length scale
$\mu$	Fluid dynamic viscosity
$\mu_\ell$	Dynamic viscosity of liquid binder
$\nu$	Fluid kinematic viscosity
$\rho$	Plume mixture density
$\rho_{amb}$	Ambient air density
$\rho_f$	Fluid density
$\rho_{ice}$	Ice density
$\rho_\ell$	Liquid water density
$\rho_m$	Tephra density
$\rho_{p,i}$	Density of particle $i$
$\rho_{i,j}^n$	Correlation coefficient of concentration fluctuations
$\sigma$	Stefan-Boltzmann constant
$\tau_\eta$	Kolmogorov time scale
$\tau_p$	Particle aerodynamic response time
$\phi$	Krumbein scale, $\phi = -\log_2(d_p/1 \text{ mm})$
$\phi_{i,j}$	Ratio of particle response times
$\chi$	Particle detrainment proportionality constant

### Conflict of Interest

The authors declare no conflicts of interest relevant to this study.

### Data Availability Statement

The PMAP model (Hoffman & Mastin, 2023) is accessible at: <https://doi.org/10.5066/P9UFXP7T>.

## Acknowledgments

This work is supported by collaborative Grants (NSF-EAR-1756068, NSF-EAR-1756259, and NSF-EAR-1756267) from the U.S. National Science Foundation. We would like to thank Graham Freedland, Kris Gish, Laura Shannon, and Bianca Viggiano for their contributions to this project. We also appreciate the suggestions of Roger Denlinger and three anonymous reviewers. Any use of trade, firm, or product names is for descriptive purposes only and does not imply endorsement by the U.S. Government.

## References

- Aubry, T., Engwell, S., Bonadonna, C., Carazzo, G., Scollo, S., Van Eaton, A., et al. (2021). The independent volcanic eruption source parameter archive (IVESPA, version 1.0): A new observational database to support explosive eruptive column model validation and development. *Journal of Volcanology and Geothermal Research*, 417, 1–31. <https://doi.org/10.1016/j.jvolgeores.2021.107295>
- Beckett, F., Rossi, E., Devenish, B., Witham, C., & Bonadonna, C. (2022). Modelling the size distribution of aggregated volcanic ash and implications for operational atmospheric dispersion modelling. *Atmospheric Chemistry and Physics*, 22(5), 3409–3431. <https://doi.org/10.5194/acp-22-3409-2022>
- Bohren, C., & Albrecht, B. (1998). *Atmospheric thermodynamics*. Oxford University Press.
- Brown, R., Bonadonna, C., & Durant, A. (2012). A review of volcanic ash aggregation. *Physics and Chemistry of the Earth*, 45–46, 65–78. <https://doi.org/10.1016/j.pce.2011.11.001>
- Bursik, M. (2001). Effect of wind on the rise height of volcanic plumes. *Geophysical Research Letters*, 28(18), 3621–3624. <https://doi.org/10.1029/2001gl013393>
- Bursik, M., Sparks, R., Gilbert, J., & Carey, S. (1992). Sedimentation of tephra by volcanic plumes: I. Theory and its comparison with a study of the Fogo A plinian deposit, Sao Miguel (Azores). *Bulletin of Volcanology*, 54(4), 329–344. <https://doi.org/10.1007/bf00301486>
- Costa, A., Folch, A., & Macedonio, G. (2010). A model for wet aggregation of ash particles in volcanic plumes and clouds: 1. Theoretical formulation. *Journal of Geophysical Research*, 115(B9), B09201. <https://doi.org/10.1029/2009jb007175>
- Costa, A., Suzuki, Y., Cerminara, M., Devenish, B., Ongaro, T., Herzog, M., et al. (2016). Results of the eruptive column model inter-comparison study. *Journal of Volcanology and Geothermal Research*, 326, 2–25. <https://doi.org/10.1016/j.jvolgeores.2016.01.017>
- Delmelle, P., Villi eras, F., & Pelletier, M. (2005). Surface area, porosity and water adsorption properties of fine volcanic ash particles. *Bulletin of Volcanology*, 67(2), 160–169. <https://doi.org/10.1007/s00445-004-0370-x>
- de' Michieli Vitturi, M., & Pardini, F. (2021). PLUME-MoM-TSM 1.0.0: A volcanic column and umbrella cloud spreading model. *Geoscientific Model Development*, 14(3), 1345–1377. <https://doi.org/10.5194/gmd-14-1345-2021>
- Durant, A., Shaw, R., Rose, W., Mi, Y., & Ernst, G. (2008). Ice nucleation and overseeding of ice in volcanic clouds. *Journal of Geophysical Research*, 113(D9), D09206. <https://doi.org/10.1029/2007jd009064>
- Eaton, J., & Fessler, J. (1994). Preferential concentration of particles by turbulence. *International Journal of Multiphase Flow*, 20, 169–209. [https://doi.org/10.1016/0301-9322\(94\)90072-8](https://doi.org/10.1016/0301-9322(94)90072-8)
- Ennis, B., Tardos, G., & Pfeffer, R. (1991). A microlevel-based characterization of granulation phenomena. *Powder Technology*, 65(1), 257–272. [https://doi.org/10.1016/0032-5910\(91\)80189-p](https://doi.org/10.1016/0032-5910(91)80189-p)
- Ernst, G., Sparks, R., Carey, S., & Bursik, M. (1996). Sedimentation from turbulent jets and plumes. *Journal of Geophysical Research*, 101(B3), 5575–5589. <https://doi.org/10.1029/95jb01900>
- Folch, A., Costa, A., Durant, A., & Macedonio, G. (2010). A model for wet aggregation of ash particles in volcanic plumes and clouds: 2. Model application. *Journal of Geophysical Research*, 115(B9), B09202. <https://doi.org/10.1029/2009jb007176>
- Folch, A., Costa, A., & Macedonio, G. (2016). FPLUME-1.0: An integral volcanic plume model accounting for ash aggregation. *Geoscientific Model Development*, 9(1), 431–450. <https://doi.org/10.5194/gmd-9-431-2016>
- Gilbert, J., & Lane, S. (1994). The origin of accretionary lapilli. *Bulletin of Volcanology*, 56(5), 398–411. <https://doi.org/10.1007/bf00326465>
- Gregory, J. (1997). The density of particle aggregates. *Water Science and Technology*, 36(4), 1–13. <https://doi.org/10.2166/wst.1997.0073>
- Gudmundsson, M., Thordarson, T., H skuldsson,  ., Larsen, G., Bj rnsson, H., Prata, F., et al. (2012). Ash generation and distribution from the April–May 2010 eruption of Eyjafjallaj kull, Iceland. *Scientific Reports*, 2(1), 572. <https://doi.org/10.1038/srep00572>
- Haar, L., Gallagher, J., & Kell, G. (1984). *NBS/NRC steam tables thermodynamic and transport properties and computer programs for vapor and liquid states of water in SI units* (No. 5614915). U.S. Department of Energy, Office of Scientific and Technical Information.
- Hoffman, D. (2022). *The role of turbulence in the aggregation of ash particles in volcanic plumes* (Doctoral dissertation). Stanford University.
- Hoffman, D., & Eaton, J. (2021). Isotropic turbulence apparatus with a large vertical extent. *Experiments in Fluids*, 62(10), 209. <https://doi.org/10.1007/s00348-021-03311-7>
- Hoffman, D., & Eaton, J. (2023). Experimental investigation of particle aggregation in a humid and turbulent environment. *International Journal of Multiphase Flow*, 163, 104423. <https://doi.org/10.1016/j.ijmultiphaseflow.2023.104423>
- Hoffman, D., & Mastin, L. (2023). PMAP software, v. 1.0.3. <https://doi.org/10.5066/P9UFXP7T>
- Jacobson, M., Turco, R., Jensen, E., & Toon, O. (1994). Modeling coagulation among particles of different composition and size. *Atmospheric Environment*, 28(7), 1327–1338. [https://doi.org/10.1016/1352-2310\(94\)90280-1](https://doi.org/10.1016/1352-2310(94)90280-1)
- Kolmogorov, A. (1941). The local structure of turbulence in incompressible viscous fluid for very large Reynolds numbers. *Doklady Akademii Nauk SSSR*, 30, 301–305.
- Kumar, S., & Ramkrishna, D. (1996). On the solution of population balance equations by discretization—I. A fixed pivot technique. *Chemical Engineering Science*, 51(8), 1311–1332. [https://doi.org/10.1016/0009-2509\(96\)88489-2](https://doi.org/10.1016/0009-2509(96)88489-2)
- Leshner, C., & Spera, F. (2015). In H. Sigurdsson, B. Houghton, S. McNutt, H. Rymer, J. Stix, & A. McBirney (Eds.), *Encyclopedia of volcanoes* (2nd ed.). Academic Press.
- Mastin, L. (2007). A user-friendly one-dimensional model for wet volcanic plumes. *Geochemistry, Geophysics, Geosystems*, 8(3), Q03014. <https://doi.org/10.1029/2006gc001455>
- Mastin, L., Schwaiger, H., Schneider, D., Wallace, K., Schaefer, J., & Denlinger, R. (2013). Injection, transport, and deposition of tephra during event 5 at Redoubt Volcano, 23 March, 2009. *Journal of Volcanology and Geothermal Research*, 259, 201–213. <https://doi.org/10.1016/j.jvolgeores.2012.04.025>
- McBride, B., Gordon, S., & Reno, M. (1993). *Coefficients for calculating thermodynamic and transport properties of individual species*. NASA Langley Research Center. (TM-4513).
- Morton, B., Taylor, G., & Turner, J. (1956). Turbulent gravitational convection from maintained and instantaneous sources. *Proceedings of the Royal Society of London. Series A. Mathematical and Physical Sciences*, 234(1196), 1–23. <https://doi.org/10.1098/rspa.1956.0011>
- Panchapakesan, N., & Lumley, J. (1993). Turbulence measurements in axisymmetric jets of air and helium. Part 1. Air jet. *Journal of Fluid Mechanics*, 246, 197–223. <https://doi.org/10.1017/s0022112093000096>
- Pope, S. (2000). *Turbulent flows*. Cambridge University Press.
- Press, W., & Teukolsky, S. (1992). Adaptive stepsize Runge-Kutta integration. *Computers in Physics*, 6(2), 188–191. <https://doi.org/10.1063/1.4823060>
- Reade, W., & Collins, L. (2000). Effect of preferential concentration on turbulent collision rates. *Physics of Fluids*, 12(10), 2530–2540. <https://doi.org/10.1063/1.1288515>
- Rossi, E. (2018). *A new perspective on volcanic particle sedimentation and aggregation* (Doctoral dissertation). Universit  de Gen ve.

- Rouse, H., Yih, C., & Humphreys, H. (1952). Gravitational convection from a boundary source. *Tellus*, *4*(3), 201–210. <https://doi.org/10.1111/j.2153-3490.1952.tb01005.x>
- Saffman, P., & Turner, J. (1956). On the collision of drops in turbulent clouds. *Journal of Fluid Mechanics*, *1*(1), 16–30. <https://doi.org/10.1017/s0022112056000020>
- Schiller, L., & Naumann, A. (1933). Über die grundlegenden Berechnungen bei der Schwerkraftaufbereitung. *Zeitschrift des Vereines Deutscher Ingenieure*, *77*, 318–321.
- Schneider, D., & Hoblitt, R. (2013). Doppler weather radar observations of the 2009 eruption of Redoubt Volcano, Alaska. *Journal of Volcanology and Geothermal Research*, *259*, 133–144. <https://doi.org/10.1016/j.jvolgeores.2012.11.004>
- Schwaiger, H., Denlinger, R., & Mastin, L. (2012). Ash3d: A finite-volume, conservative numerical model for ash transport and tephra deposition. *Journal of Geophysical Research*, *117*(B4), B04204. <https://doi.org/10.1029/2011jb008968>
- Smoluchowski, M. (1918). Versuch einer mathematischen Theorie der Koagulationskinetik kolloider Lösungen. *Zeitschrift für Physikalische Chemie*, *92*, 128–168.
- Sorem, R. (1982). Volcanic ash clusters: Tephra rafts and scavengers. *Journal of Volcanology and Geothermal Research*, *13*(1), 63–71. [https://doi.org/10.1016/0377-0273\(82\)90019-1](https://doi.org/10.1016/0377-0273(82)90019-1)
- Sparks, R., Bursik, M., Carey, S., Gilbert, J., Glaze, L., Sigurdsson, H., & Woods, A. (1997). *Volcanic plumes*. Wiley.
- Sundaram, S., & Collins, L. (1997). Collision statistics in an isotropic particle-laden turbulent suspension. Part I. Direct numerical simulations. *Journal of Fluid Mechanics*, *335*, 75–109. <https://doi.org/10.1017/s0022112096004454>
- Textor, C., & Ernst, G. (2004). Comment on “Particle aggregation in volcanic eruption columns” By Graham Veitch and Andrew W. Woods. *Journal of Geophysical Research*, *109*, B05202. <https://doi.org/10.1029/2002jb002291>
- Van Eaton, A., Mastin, L., Herzog, M., Schwaiger, H., Schneider, D., Wallace, K., & Clarke, A. (2015). Hail formation triggers rapid ash aggregation in volcanic plumes. *Nature Communications*, *6*(1), 7860. <https://doi.org/10.1038/ncomms8860>
- Veitch, G., & Woods, A. (2001). Particle aggregation in volcanic eruption columns. *Journal of Geophysical Research*, *106*(B11), 26425–26441. <https://doi.org/10.1029/2000jb900343>
- Wallace, K., Schaefer, J., & Coombs, M. (2013). Character, mass, distribution, and origin of tephra-fall deposits from the 2009 eruption of Redoubt Volcano, Alaska—Highlighting the significance of particle aggregation. *Journal of Volcanology and Geothermal Research*, *259*, 145–169. <https://doi.org/10.1016/j.jvolgeores.2012.09.015>
- Woods, A. (1988). The fluid dynamics and thermodynamics of eruption columns. *Bulletin of Volcanology*, *50*(3), 169–193. <https://doi.org/10.1007/bf01079681>
- Woods, A. (1993). Moist convection and the injection of volcanic ash into the atmosphere. *Journal of Geophysical Research*, *98*(B10), 17627–17636. <https://doi.org/10.1029/93jb00718>
- Zhou, Y., Wexler, A., & Wang, L. (2001). Modelling turbulent collision of bidisperse inertial particles. *Journal of Fluid Mechanics*, *433*, 77–104. <https://doi.org/10.1017/s002211200003372>